Accepted Manuscript
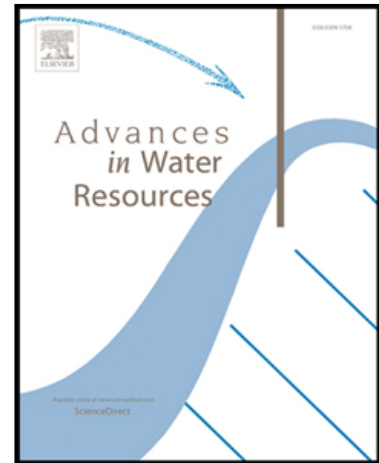
DYNAMIC PORE-SCALE NETWORK MODEL (PNM) OF WATER IMBIBITION IN POROUS MEDIA

J. Li , S.R. McDougall , K.S. Sorbie

Please cite this article as: J. Li , S.R. McDougall , K.S. Sorbie , DYNAMIC PORE-SCALE NETWORK MODEL (PNM) OF WATER IMBIBITION IN POROUS MEDIA, *Advances in Water Resources* (2017), doi: 10.1016/j.advwatres.2017.06.017

Highlights:

- Introduction Section has been revised and additional references have also been added. Especially a review concerning the one-pressure and two-pressure algorithmic approaches, which are used to account for the influence of wetting films, has been added on page 6.

- Figures illustrating the evolution and distribution of local switch have been added in Section III (b) and (c). (Figure 9, 10, 12, 15, 16, 17, 18, 19, 20).

- 3D results, including the relative permeability curves, and related discussions have been add in Section III (b). (Figure 11 - 14).

- We have rearranged the structure of Section III and have added some 3D results in Section III (b), including the global pressure drop, water fractional flow and relative permeability. Therefore, the former Section III (c) has become redundant and has been removed.

- Model validation has been discussed on Page 45.

1

DYNAMIC PORE-SCALE NETWORK MODEL (PNM) OF WATER IMBIBITION IN POROUS MEDIA

J. Li, S. R. McDougall, K. S. Sorbie

Institute of Petroleum Engineering, Heriot-Watt University, Edinburgh, EH 14 4AS, UK

ABSTRACT

A dynamic pore-scale network model is presented which simulates 2-phase oil/water displacement during water imbibition by explicitly modelling intra-pore dynamic bulk and film flows using a simple local model. A new dynamic switching parameter, λ, is proposed within this model which is able to simulate the competition between local capillary forces and viscous forces over a very wide range of flow conditions. This quantity (λ) determines the primary pore filling mechanism during imbibition; i.e. whether the dominant force is (i) piston-like displacement under viscous forces, (ii) film swelling/collapse and snap-off due to capillary forces, or (iii) some intermediate *local* combination of both mechanisms.

A series of 2D dynamic pore network simulations is presented which shows that the λ-model can satisfactorily reproduce and explain different filling regimes of water imbibition over a wide range of capillary numbers (Ca) and viscosity ratios (M). These imbibition regimes are more complex than those presented under drainage by Lenormand and coworkers (Lenormand and Zarcone (1983)), since they are determined by a wider group of control parameters. Our simulations show that there is a coupling between viscous and capillary forces that is much less important in drainage. The effects of viscosity ratio during imbibition are apparent even under conditions of very slow flow (low Ca) − displacements that would normally be expected to be completely capillary dominated. This occurs as a result of the wetting films having a much greater relative mobility in the higher M cases (e.g. $M = 10$) thus leading to a higher level of film swelling/snap-off, resulting in local oil cluster bypassing and trapping, and hence a poorer oil recovery. This deeper coupled viscous mechanism is the underlying reason why the microscopic displacement efficiency is lower for higher M cases in water imbibition processes.

Additional results are presented from the dynamic model on the corresponding effluent fractional flows (f_w) and global pressure drops (ΔP) as functions of capillary number and viscosity ratio. These results indicate that unsteady-state (USS) relatively permeabilities in imbibition should be inherently rate dependent.

Key words: dynamic model; pore-scale network model; imbibition; porous media; capillary forces; viscous forces.

I.   INTRODUCTION

In oil reservoir engineering and contaminant transport, macroscopic properties such as capillary pressures and relative permeabilities are of great importance, since they are required as functions to carry out future predictions of oil recovery from a hydrocarbon reservoir or aquifer remediation following contamination. However, these quantities are difficult and expensive to obtain and, even when they are measured experimentally, there are a number of associated uncertainties. Indeed, when experiments using rock samples from the actual reservoir are possible, the results may only reflect the flow functions under specific conditions (viscous/capillary ratios).

Therefore, more physically based models are needed to understand, simulate and predict multiphase flow behaviour in porous media. Ideally, these models should be based on an understanding of the pore scale fluid displacement physics of the flow process of interest (e.g. water flooding) since all processes in an oil reservoir must ultimately relate back to this micro-scale. The first pore network model (PNM) for simulating two phase flow behaviour was developed by Fatt in the 1950s (Fatt, (1956a, 1956b, 1956c)). Using the Young-Laplace equation, Fatt filled the pores and throats in a regular 2D lattice in the order of inscribed radius and produced qualitative forms of capillary pressure and relative permeability curves. Since then, especially since the late 1970s when computer processing power became more readily available, the use of pore network models as investigative tools to study multiphase flow from the pore (μm) to core (mm to cm) scale has grown.

Generally, there are two types of pore-scale network models: quasi-static and dynamic PNMs. In quasi-static models, capillary pressure is the dominant force and the positions of all fluid-fluid interfaces can be determined at each stage of the displacement. Quasi-static models can be considered as extensions of simple percolation models, with drainage floods being modelled through invasion percolation and imbibition through adapted bond percolation processes. In invasion percolation drainage models, the invading fluid fills a pore or throat in order of its size (more strictly in order of its increasing capillary entry pressure − which may involve wettability through the contact angle), and there may also be conditions of "accessibility" of the pore/throat object. Quasi-static models ignore rate effects and they

have produced a number of results which are in good qualitative agreement with laboratory measured relative permeabilities (e.g. see McDougall and Sorbie (1994, 1995); Blunt et al. 1997a, 1997b; Valvatne (2004); Øren et al. (1998); Man and Jing (1999); Ryazanov et al. (2009)).

In *dynamic* pore network models, an explicit time scale must be introduced for pore filling events and the emergent rate-dependent flow regimes are determined by the competition between capillary forces and viscous forces. Several dynamic pore network models have been described in the literature that simulate unsteady-state displacements in porous media in different ways (e.g. Aker et al. (1998), Mogensen and Stenby (1998), Singh and Mohanty (2003), Hughes and Blunt (2000), Al-Gharbi and Blunt (2005), Nguyen et al. (2006), Idowu (2009)). Of these models, Mogensen and Stenby (1998), Singh and Mohanty (2003), Hughes and Blunt (2000) represented the porous medium by a network consisting of wide pores connected by throats; Al-Gharbi and Blunt (2005) applied a similar network structure, but the inscribed radius of a pore or a throat varied sinusoidally; Nguyen et al. (2006) and Idowu (2009) conducted their simulations in a network generated from a Berea sandstone; whilst Aker et al. (1998) used a network structure in which the pores they used were hourglass shaped. Below, we present a brief comparative review of the various dynamic pore-scale models that have been published to date, and compare them with our new model (full details of this dynamic model are described in Li (2016)) in three main aspects: (i) on the displacement mechanisms included (Table 1), (ii) on the fluid configuration considered (Table 2), and (iii) on the methods used to implement the viscous-capillary force balance and hence the ability of the model to simulate rate-dependency.

Lenormand and Zarcone (1984) described the displacement processes operating during imbibition in terms of piston-like displacement, snap-off, and pore body filling I_z mechanisms. The model of Aker et al. (1998) only simulated piston-like displacement in drainage, whilst the models of Mogensen and Stenby (1998), Singh and Mohanty (2003), and Al-Gharbi and Blunt (2005) concentrated on piston-like displacement and snap-off only. Other models (Hughes and Blunt (2000), Nguyen et al. (2006), Idowu (2009)) have included all three mechanisms: piston-like displacement, snap-off, and I_z mechanism (Table 1).

In addition to piston-like displacement and snap-off mechanisms, our newly proposed dynamic model includes the coupling of bulk advancement and film swelling, allowing us to simulate intermediate cases where these two mechanisms are coupled and possibly quite

closely balanced. This is an important extension to earlier approaches and allows us to better account for the rate-dependency seen in dynamic imbibition.

Table 1 Pore-level events included in dynamic models

Model	Pore-level events			
	Piston-like displacement	Snap-off	I_z mechanism	Coupling of bulk and film
Aker et al. (1998)	√			
Mogensen and Stenby (1998)	√	√		
Hughes and Blunt (2000)	√	√	√	
Singh and Mohanty (2003)	√	√		
Al-Gharbi and Blunt (2005)	√	√ (throat)		
Nguyen et al. (2006)	√	√	√	
Idowu (2009)	√	√	√	
This work	√	√		√

In line with the pore-level events simulated by each model, the corresponding fluid configurations are illustrated in Table 2. Aker et al. (1998) simulated moving bulk menisci during piston-like displacement in drainage and ignored wetting films. In other models (Mogensen and Stenby (1998); Hughes and Blunt (2000); Singh and Mohanty (2003)), no moving bulk menisci were simulated; corner flow in these models tended to have fixed thickness and conductance (usually chosen by users), which effectively prevented the wetting film from swelling (although snap-off was allowed under suitable conditions). In Nguyen et al. (2006) and Idowu (2009) models, although there is still no mobile bulk meniscus, film volumes were updated based on the local sorting capillary pressure. Al-Gharbi and Blunt (2005) updated the locations of bulk interfaces to account for local volume change and swelling films were also simulated – however, the technique used was only viable in a specific network structure.

The dynamic model described here will update the movement of bulk menisci *and* the thickness of wetting films at each time step, simulating both piston-like displacement and

film swelling simultaneously, where appropriate. The method used to update fluid configuration (bulk and film) is based on the local flux and time step, which is more physical than previous models and can be easily adapted to any network structure. Furthermore, this new filling mechanism (coupling of bulk and film) models an important fluid configuration (as seen in Table 2) – a switch parameter λ is used to distribute incoming displacement fluid (water) appropriately. Phase conductances, local/global pressure drops and flow rates are all updated accordingly.

Table 2 Fluid configurations described in various dynamic models

Model	Fluid configurations				
	(a) Bulk		(b) Film		(c) Bulk and Film
	Fixed	Updated	Fixed	Updated	
Aker et al. (1998)		√			
Mogensen and Stenby (1998)	√		√		
Hughes and Blunt (2000)			√		
Singh and Mohanty (2003)			√		
Al-Gharbi and Blunt (2005)		√		√	
Nguyen et al. (2006)				√	
Idowu (2009)				√	
This work		√		√	√

In a quasi-static model, fluid displacement is controlled only by capillary forces, while in a dynamic model, viscous forces are also included and the displacement regime is rate-dependent. Generally speaking, for dynamic models, there are two methods to implement

viscous forces in pores with bulk menisci (as seen in Table 2 (a)). The first method for implementing viscous forces is to include the viscous pressure or flow rate into the sorting pressure, which will be used to rank and fill all the pore elements (Hughes and Blunt (2000); Nguyen et al. (2006); Idowu (2009)). Based on the particular definition of the sorting pressure, events (bulk displacement or snap-off) with the highest/lowest sorting pressure will be executed first. The sorting pressure actually works in the same way as the global capillary pressure in the quasi-static model and models applying this method are intermediate methods between quasi-static and fully dynamic approaches.

The second is to add capillary entry pressure terms when calculating local flow rates in pores containing *bulk menisci* during the process of updating pressure field (Aker et al. (1998); Mogensen and Stenby (1998); Singh and Mohanty (2003); Al-Gharbi (2004)) . Of these models, Aker et al. (1998) and Singh and Mohanty (2003) only considered bulk displacement during drainage displacements; Mogensen and Stenby (1998) included snap-off events based on the throat to pore aspect ratio and then determined the event that would happen first by comparing the filling time via bulk displacement and snap-off. In the model proposed by Al-Gharbi (2004), additional isolated water clusters emerged during simulations at low capillary number, since the wetting layers had sufficient time to swell and cause snap-off.

Furthermore, there are also two approaches for solving the pressure field that account for the influence of wetting films (Table 2 (b)): single-pressure algorithm and two-pressure algorithm (a detailed discussion can be found in Joekar-Niasar and Hassanizadeh (2012)). In the single-pressure algorithm case, a single pressure is assigned to each pore regardless of the fluid occupancy based on one of three possible assumptions: 1. pore body or pore throat can only be occupied by bulk phase, often applied to networks with circular pores (Aker et al. (1998)); 2. both phases can be present in a pore body but not in a pore throat, and the local capillary pressure in pore bodies is assumed negligible (see Blunt and King, 1990; Gielen et al., 2005); 3. an equivalent fluid with averaged conductance is used to represent the two fluids present within a pore element (Mogensen and Stenby (1998), Singh and Mohanty (2003), Al-Gharbi and Blunt (2005)). In the two-pressure algorithm, for a pore occupied by both fluids (e.g. wetting film and bulk fluid), the mass balance and pressure of each fluid are solved separately (but coupled) (see Thompson (2002), Joekar-Niasar et al. (2010a)). Joekar-Niasar et al. (2010a) and Joekar-Niasar and Hassanizadeh (2011) have improved the two-pressure algorithm to reduce the computational demand.

The new dynamic model proposed here will include capillary entry pressure terms in the pressure solution, and apply the one-pressure algorithm under assumption 3 above. In addition, a rate-dependent switch parameter λ will be used to distribute the incoming displacing phase (water) within the pores, with both a moving meniscus *and* swelling films where appropriate − this represents the local competition between piston-like displacement and snap-off.

We begin with a description of the new dynamic pore-scale network model of imbibition. This model considers capillary entry pressure in pores with bulk menisci and introduces the coupled filling mechanism of piston-like displacement and snap-off to implement viscous forces and simulate rate-dependency. Using the dynamic switching parameter, λ, this model is able to simulate the competition between capillary forces and viscous forces under a wide range of flow conditions and determine the primary filling mechanism *automatically*. Bulk menisci movement and film swelling are simulated through a more physical flux-based algorithm and a detailed *Depth-First Search* (*DFS*) backtracking algorithm has been applied to identify all oil-trapped pores based on both topology and local flow direction. The model has been implemented in 2D and 3D pore scale network models and the wettability of the pore is described by the contact angle (θ_{ow} or cos θ_{ow}). The network is composed of triangular cross-section bonds and volume-less nodes; the nodes were omitted, since even the static (I_z) pore body filling mechanism has not been rigorously established and no dynamic filling model is known (the three models including (I_z) pore body filling mechanism (Hughes and Blunt (2000); Nguyen et al. (2006); Idowu (2009)) use quasi-static-like sorting pressure to implement viscous forces and are not fully dynamic models).

2D and 3D results will be presented to illustrate influence of the local capillary/viscous force balance (λ) during network flow. Example 2D dynamic simulations will also be presented to illustrate the flow regimes that emerge as functions of flow rate and mobility ratio in imbibition. Results demonstrate that rate dependency is clearly observed in outlet fractional flows (f_w) and network global pressure drops (ΔP), indicating that imbibition relative permeabilities are rate dependent. A more detailed description of the model is reported in Li (2016), together with an exhaustive series of simulation results.

II.   DYNAMIC PORE-SCALE NETWORK MODELS OF IMBIBITION

a) Network Structure and Boundary Conditions

The porous medium is represented as a distorted 2-D or 3-D lattice of pore elements that are connected to one another through volume-less nodes. The filling rules at nodes in a pore network model is usually described by (I_z) pore body filling mechanisms (Lenormand and Zarcone (1984), Blunt et al. 1997a, 1997b; Ryazanov et al. (2009)) and, whilst this has proved to be a simple and useful approach to pore body filling, it is not rigorously established and no corresponding dynamic filling model is known. Therefore, we choose to work with volume-less nodes and bond only lattices and demonstrate that, even under these simplifying assumptions, a rich behaviour of unsteady-state imbibition is observed.   The size of the network is given by the number of nodes in three directions which are denoted as n_x, n_y, n_z and all of the pores randomly assigned an inscribed radius (r) and a length (l).

To accommodate the possibility of active wetting films, angular pores are introduced into the dynamic model – specifically, pores with triangular cross sections (although other pores shapes could be considered straightforwardly).

In the triangular pore model, the cross-sectional shape is characterized by the radius r of the inscribed circle and the half-angles of three corners and for a generalised triangle is given by the equation

$$A_t = r^2 \sum_{i=1}^{3} \frac{1}{\tan \beta_i} \qquad\qquad 1$$

where $\beta_1 \geq \beta_2 \geq \beta_3$, $\beta_1 + \beta_2 + \beta_3 = 90^o$ are the half angles.

The treatment of angular pores, especially the wetting films in pore corners (water is present as arc menisci (*AMs*)), is based on work of Oren et al. (1998) and Valvatne (2004):

Now the corner area occupied by wetting films is given by:

$$A_w = r_w^2 \sum_{i=1}^{n} [\frac{\cos\theta \cos(\theta + \beta_i)}{\sin \beta_i} + \theta + \beta_i - \frac{\pi}{2}] \qquad\qquad 2$$

where θ is the contact angle, $r_w = \sigma/P_c$ is the radius of curvatures of the *AMs*, and n is the number of corners that host corner water.

If we define

$$S_1 = \sum_{i=1}^{n} [\frac{\cos\theta\cos(\theta+\beta_i)}{\sin\beta_i} + \theta + \beta_i - \frac{\pi}{2}],$$ 3

then the corner water area can be written as

$$A_w = r_w^2 \cdot S_1.$$ 4

The area of the central part of a pore occupied by bulk non-wetting fluid follows immediately:

$$A_{nw} = A_t - A_w$$ 5

Note here that, unlike in quasi-static models, there is no specific global capillary pressure in the dynamic model to determine the cross-sectional area occupied by corner water. In fact, the dynamic model records the local fluid configuration as a function of time and calculates local meniscus curvature r_w through the current wetting film thickness:

$$r_w = \sqrt{A_w / S_1} .$$ 6

And so capillary pressure varies spatially and temporally as the flood proceeds. It should also be noted that the number of *AMs* does not always match the number of corners – indeed, for a particular corner with half angle β, if $\theta \geq 90^o - \beta$, this corner will contain no water at all. Therefore, in a particular pore element, the value of contact angle will determine both the number and curvature of its associated *AMs*.

Our dynamic model focuses on water imbibition, where the injected water flows into the system at constant flow rate from the left side of the model (inlet) towards the right side of the model (outlet): no-flow boundary conditions are imposed on all other faces of the system. Gravity effects are neglected and the pressure difference between the model inlet and outlet defines the pressure drop across the network – note that this will change during a displacement due to changes in fluid configuration under constant flow rate conditions.

b) Pore-level Events

For ease of discussion, we will use the term "oil" in what follows as a shorthand for the non-wetting phase, although this can be considered a cipher for any non-aqueous phase liquid

10

(NAPL). During laboratory water injection experiments, water is usually injected from the network inlet at a constant rate and displaces a defending oil phase occupying the centre of water-wet pores. Water-wet triangular pores will initially have water in their corners as wetting films and the imbibition mechanism will generally be more complex compared with primary drainage and will consist of both piston-like and snap-off mechanisms (Lenormand et al, (1983)).

Piston-like Displacement

For piston-like displacement (Figure 1), water will flow into the pore element forming a bulk water/oil meniscus perpendicular to the flow direction. In the calculation of the global pressure field and local flow rates, this mechanism requires a capillary pressure term to be taken into account, which will always help the displacement in imbibition (in contrast to drainage). All of our simulations are conducted in water-wet systems (the value of contact angle is constant and not above 90°) and so, in most cases, piston-like displacement can occur in each pore as long as there is *upstream* adjacent bulk water available (in water-filled neighbouring pores or at the system inlet). To avoid the retreat of menisci, pores with a counter-current flow direction are considered to be viable over the current time step, i.e. the bulk meniscus can only penetrate and advance if $\Delta P > -P_c$, where ΔP is the pressure drop from the water-filled end to the oil-filled end of the pore.
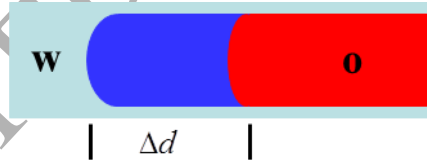

Figure 1 Illustration of the bulk menisci advancing.
Blue (both light and dark) is water, red is oil; dark blue represents the water volume increment in the displacement.

Now, in each pore, considering water influx and efflux, q_w^{in} and q_w^{out}, the water volume increment associated with that pore, ΔV_w is:

$$\Delta V_w = (q_w^{in} - q_w^{out}) \cdot \Delta t \qquad\qquad 7$$

where, for piston-like events, q_w^{in} is equal to the total influx, and water can only escape from these pores through wetting films.

Defining Δd as the incremental distance the bulk meniscus has travelled along a pore during the current time step Δt, and A_o the oil-occupied cross-sectional area, all of the incremental water is used to propel the bulk meniscus through the oil (Figure 1), i.e.

$$\Delta d = \Delta V_w / A_o \qquad\qquad 8$$

and once a pore is fully-filled by water, the bulk meniscus can then move into all adjacent downstream oil-filled pores.

In this model, the capillary entry pressure for piston-like displacement in an angular pore is calculated using the equations proposed in Valvatne (2004):

$$P_c^{piston-like} = \frac{\sigma_{ow} \cos\theta (1 + 2\sqrt{\pi G_{shape}})}{r} \cdot F_d(\theta_r, G_{shape}, \beta) \qquad\qquad 9$$

where θ is the contact angle, G_{shape} is the shape factor, σ is the interfacial tension (IFT), and

$$F_d(\theta_r, G_{shape}, \beta) = \frac{1 + \sqrt{1 - \dfrac{4G_{shape}S_1}{\cos^2\theta_r}}}{(1 + 2\sqrt{\pi G_{shape}})} , \qquad\qquad 10$$

where S_1 is given by Equation 3.

If we now define

$$F_d^{piston-like} = \cos\theta + \sqrt{\cos^2\theta - 4G_{shape}S_1} , \qquad\qquad 11$$

then Equation 9 and 10 can be manipulated and the capillary pressure can be written as

$$P_c = \frac{F_d^{piston-like} \cdot \sigma_{ow}}{r} . \qquad\qquad 12$$

Film Swelling and Snap-off

In angular pores, water will accumulate in corners and wetting films can expand as water flows along the pore edges – if it swells sufficiently, so that the fluid/fluid interface becomes unstable, then snap-off occurs.
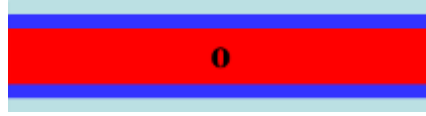
Figure 2 Illustration of the film swelling.

Blue (both light and dark) is water, red is oil; dark blue represents the water volume increment in the displacement.

The existence of a good water supply near the inlet of the network means that wetting films in upstream untrapped pores will swell first and subsequently act as new water sources to expand downstream films. In a given pore element, different water flows q_w^{in} and q_w^{out} at the pore inlet and outlet will again alter the water volume as shown in Equation 7.

For pure film swelling, the entire increment will be used to grow the water residing in pore corners, and so:

$$\Delta A_o = -\Delta V_w / l \qquad\qquad 13$$

In each pore, q_w^{in} and q_w^{out} are determined by the pore-level fluid configurations and surrounding conditions; details of how the specific water flows are obtained will be given later.

The capillary pressure at which snap-off occurs is lower than that of piston-like displacement due to the morphology of the associated meniscus (Valvatne (2004)) and is given by:

$$P_{c,entry}^{snap-off} = \frac{\sigma}{r_{w,\min}^{snap-off}} \qquad\qquad 14$$

where $r_{w,\min}^{snap-off}$ is the radius of curvature of *AMs* when snap-off occurs.

Based on the number of merging *AMs* when snap-off occurs, $r_{w,\min}^{snap-off}$ is given by:

13

$$r_w^{snap-off} = \begin{cases} r \cdot \dfrac{\dfrac{\cos \beta_1}{\sin \beta_1} + \dfrac{\cos \beta_3}{\sin \beta_3}}{\dfrac{\cos(\theta + \beta_3)}{\sin \beta_3}}, & 1\ AM \\[2em] r \cdot \dfrac{\dfrac{\cos \beta_2}{\sin \beta_2} + \dfrac{\cos \beta_3}{\sin \beta_3}}{\dfrac{\cos(\theta + \beta_2)}{\sin \beta_2} + \dfrac{\cos(\theta + \beta_3)}{\sin \beta_3}}, & 2\ \text{or}\ 3\ AMs \end{cases}$$

15

where $\beta_1 \geq \beta_2 \geq \beta_3$. If we denote

$$F_d^{snap-off} = \frac{r}{r_w^{snap-off}},$$

16

the corresponding capillary entry pressure for snap-off will be:

$$P_{c,entry}^{snap-off} = \frac{F_d^{snap-off} \cdot \sigma}{r}.$$

17

Given the capillary pressure for piston-like displacement is larger than that of snap-off in the same pore, the former is always more likely to happen when it is topologically possible and snap-off can only occur in elements that are without an immediately available bulk water supply. As snap-off does not require adjacent upstream bulk water, it can occur anywhere in the network as long as the water supply is adequate and oil is not trapped by the wetting phase.

The water configuration when dominated by piston-like displacements leads to continuous bulk water paths from the network inlet. However, snap-off will generate scattered clusters of water-filled pores which may cause increased trapping of the oil phase.

Coupling of Piston-like Advancement and Film Swelling

In a dynamic displacement, pore elements can be found in various intermediate states before becoming fully filled; *i.e.* there may be partially-filled pores with water/oil menisci partly intruded into the pore together with possible corner water (see Figure 3).

Hence, bulk menisci advancement and wetting film swelling will co-exist in a dynamic imbibition model and the rate-dependent competition between these two mechanisms is

14

determined by the dominating force, either viscous or capillary. In each pore, the existence of a partially advanced water/oil meniscus is solely determined by the presence of bulk water in an *upstream adjacent* node and is independent of injection rate. However, local fluid velocity will affect the precise water partition (between piston like advance and film flow) after the bulk meniscus has partially penetrated the pore. At high-rates, where the viscous force is more dominant, a large portion of the water would be expected to stay in the pore centre, pushing the meniscus along the pore with negligible film swelling, as in Figure 3 (a). Conversely, at low-rates, capillary forces dominate and most of the incoming water would tend to swell the water films, as in Figure 3 (b).

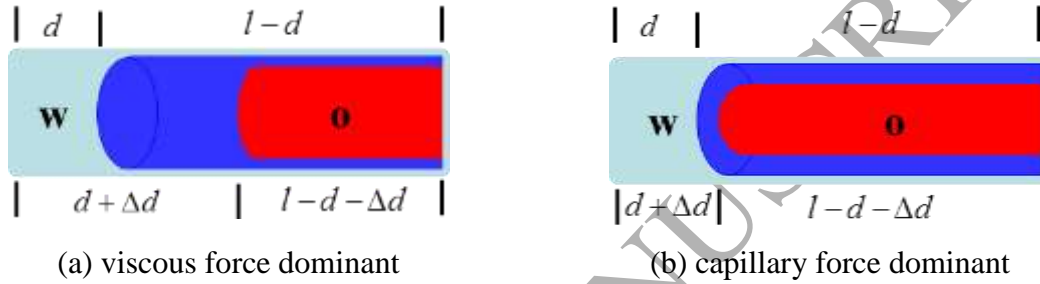(a) viscous force dominant   (b) capillary force dominant

Figure 3 Illustration of the coupled piston-like/film swelling displacement mechanisms
Light blue denotes the previous water configuration, dark blue shows the updated
configuration due to entering water, red denotes oil.

To capture the aforementioned scenarios, a local force balance 'switch', λ, has been introduced in each element to describe the competition between viscous and capillary forces. We define this switch as follows:

$$\lambda = \frac{P_c}{P_c + \Delta P}$$

18

where P_c is the capillary entry pressure in the particular element, and ΔP is the viscous pressure drop across the same pore (from the water-filled end to the oil-filled end). Note here that the switch λ is assumed to represent the *linear* relationship between P_c and ΔP – sensitivity research may be conducted later to find out if there is a better analytical form that better matches experiment. The qualitative trend of any improved switch model, no matter how non-linear, would still be in the same *direction* however (λ = 0 → viscous forces dominate, λ = 1 → capillary forces dominate) and would be trivial to implement. However, from numerical experiments (presented below) we find that this form leads to a rich range of

15

emergent behaviour and seems to be sufficient to provide some clear predictions about the possible flow regimes for imbibition.

Whenever bulk water flows into a pore, the switch λ can be used to partition the water increment as follows:

$$V_o^{new} = V_o^{old} - \Delta V_w, \qquad\qquad 19$$

$$A_o^{new} = A_o^{old} - \frac{\Delta V_w \cdot \lambda}{l - d^{old}}, \qquad\qquad 20$$

$$d^{new} = l - \frac{V_o^{new}}{A_o^{new}}. \qquad\qquad 21$$

From the above equations, it can be seen that the value of λ is positively correlated to the extent of film swelling, with $\lambda = 1$ giving only film swelling (capillary dominated) and $\lambda = 0$ giving pure piston like advance (viscous dominated). Therefore, as well as representing the competition between capillary and viscous forces, this switch also controls the distribution of incoming water in accordance with the favoured filling mechanism.
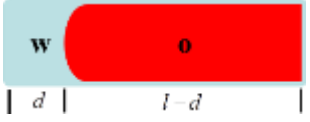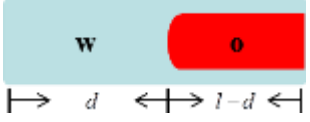
c) Fluid Configuration and Conductance

Different filling mechanisms determine the various pore-level fluid configurations and four possible wetting fluid configurations have been identified and included in the dynamic model proposed here: 1. fully-filled with water; 2. oil filled with a wetting film and no bulk meniscus; 3. partially filled with a bulk meniscus and negligible film; and 4. partially filled with both a bulk meniscus and a wetting film (these are summarised in Table 3).

Table 3 Fluid configurations and total conductance.

Blue denotes water and red denotes oil

No.	Configuration	Conductance
1	w	$g = \dfrac{G_w}{l}$
2	o	$g = \dfrac{G_w}{l} + \dfrac{G_o}{l}$

3		$g = \dfrac{1}{\dfrac{d}{G_w} + \dfrac{l-d}{G_o}}$
4		$g = \dfrac{1}{\dfrac{d}{G_{w,bulk}} + \dfrac{l-d}{G_o + G_{w,film}}}$

The hydraulic conductance is clearly strongly determined by the local fluid distribution and calculating the fluid conductance is a complicated problem for some of these configurations. Here, we adapt the approach of Al-Gharbi and Blunt (2005), using an equivalent electrical resistor network to help simplify the computations – pore-scale hydraulic conductances for each fluid configuration are listed in Table 3, where G_i is the conductance in each region per unit length and the subscript i stands for oil or water based on the particular case (see below).

Pores in this model are assigned triangular cross-sections and fixed inscribed radii, and so the general form of the fluid hydraulic conductance, g, over a length (x) can be written as:
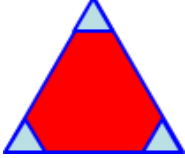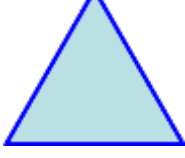
$$g = \frac{G_i}{x}.$$ 22

where x can be l, d, or $l-d$ depending upon the specific fluid configuration of interest.

Considering film swelling and snap-off, water can exist in four possible *cross-sectional* configurations: in a pore containing a mobile film, water will initially exist in pore corners as thin and stable lenses (Table 4 (i)) that will gradually swell until two or more *AMs* meet or one *AM* reaches the pore corner (Table 4 (ii)). At this point, "spontaneous" water filling occurs (Table 4 (iv)), although it is possible that snap-off in some pores cannot finish during a particular time step and so Table 4 (iii) is used to describe this intermediate state – the meniscus is unstable but there is currently insufficient water available to complete the snap-off event. In our model, conductance per unit length for each phase (G_w and G_o) in non-circular geometries follows the development of Oren et al. (1998). Note also that the local corner meniscus radius of curvature can be inferred from Equation 6 ($r_w = \sqrt{A_w/S_1}$).

17

Table 4 Cross-sectional fluid configuration and water conductance.

Blue denotes water and red denotes oil

No.	Configuration	G_w
(i)		$G_w^i = \dfrac{A_w^2}{C_w \mu_w S_1}$ (1)
(ii)		$G_w^{ii} = \dfrac{(A - A_o^{snap-off})^2}{C_w \mu_w S_1}$ (2)
(iii)		$G_w^{iii} = G_w^{ii} + \dfrac{A_o^{snap-off} - A_o}{A_o^{snap-off}} \cdot (G_w^{iv} - G_w^{ii})$ (3)
(iv)		$G_w^{iv} = \dfrac{3r^2 A}{20 \mu_w}$

Note (1): C_w is a dimensionless flow resistance factor which accounts for the reduced water conductivity close to the pore walls (notionally accounting for wall surface roughness and zero slip boundaries). *We initially assume C_w is equal in all the corners with AMs, and assign it a relatively large value ($O(10^2)$ compared with 20/3 in the bulk conductance formula)*, and so, for the corners and bulk with identical cross-sectional area, the corner conductance is appreciably smaller than the bulk value, in keeping with reality.

Note (2): $A_o^{snap-off}$ is the area occupied by bulk oil when snap-off occurs.

Note (3): G_w^{iii} is the sum of G_w^{ii} and the volume-weighted ring-region conductance.

For all of the above cases with bulk oil, the formula to calculate the conductance of non-wetting phase is $G_o = (3r^2 A_o)/(20 \mu_o)$.

d) Updating the Pressure and Flow Field

Although mass conservation at each volume-less node implies:

$$\sum q_{ij} = 0 \qquad\qquad 23$$

18

mass conservation of water cannot be considered alone since it is the gradient of water flow that drives the film swelling process in downstream pore elements. It is the balance of *total* flow that must be maintained and so the pressure field is updated by considering the total (oil plus water) flow at each node.

In pores without bulk menisci, the local flow rate is computed by assuming a Poiseuille-type relationship between the flow rate q and the pressure gradient as follows:

$$q = g \cdot (P_i - P_j). \qquad\qquad 24$$

In pores containing transverse menisci, capillary pressure must be introduced into the calculation of local flow rate and so:

$$q = g \cdot (P_i - P_j + P_c) \qquad\qquad 25$$

where P_i is the nodal pressure at the water-filled end of the pore and P_j is the nodal pressure of the oil-occupied end. Applying the above formulae in each pore and mass conservation at each node, we obtain a set of linear equations and, by solving these, the pressure field and flow field can be updated. Note that the sign of the flow represents the flow direction and the capillary pressure that helps move the bulk menisci should have the same sign as the flow from water to oil.

This model primarily considers dynamic water flooding at constant flow rate. Therefore as the displacement proceeds, the changing fluid configurations require a constant adjustment of the global pressure drop to maintain this predefined injection rate. The method introduced by Aker et al (1998) has been implemented in our model. In Aker's method, the governing equation $Q = a(\Delta P + \overline{P}_{c,entry}) = a\Delta P + b$ is linear. However, in actual simulations, especially when the constant injection rate is low, a and b in this equation are highly sensitive to the assigned pressure drop and may change accordingly. Therefore this method, which involves an initial guess of pressure drop, must be iterated until the injection rate is equal to the predefined rate within a specified accuracy.

In low rate cases, where capillary forces play a more important role, negative flows at the network inlet/outlet may occur. These phenomena can sometimes be seen in laboratory experiments and cause problems in the subsequent calculation of relative permeability. To simplify the relative permeability calculation, we iterate the pressure solution; first, we check

19

the flow direction of all network inlet/outlet pores at each time step, temporarily close pores characterised by negative flows and temporarily remove them from the conductivity matrix, re-solve the pressure field, and repeat. At the end of this iterative procedure, we end up with a pressure drop that is consistent with the fixed injection rate and configuration of open pores.

e) Determining the local water flow

It is important that the water influx and efflux associated with each pore are treated separately, since the water flow gradient they create will be used to update the local volumetric water changes. Now, based on the explicit fluid configuration in each pore, local water influx (q_w^{in}) and efflux (q_w^{out}) can be calculated as indicated in Table 5.

Table 5 q_w^{in} and q_w^{out} in pores with explicit fluids configuration.

Blue denotes water, red denotes oil.

No.			a	b	c
Configuration			w	o	w o
Water Film Untrapped	Oil Untrapped	q_w^{in}	q	$q \cdot \dfrac{g_w}{g}$	q
		q_w^{out}	q	$q \cdot \dfrac{g_w}{g}$	$q \cdot \dfrac{G_{w,film}}{G_{w,film}+G_o}$
	Oil Trapped	q_w^{in}	NA	q	q
		q_w^{out}		q	q
Water Film Trapped	Oil Untrapped	q_w^{in}	NA	0	q
		q_w^{out}		0	0
	Oil Trapped	q_w^{in}		0	0
		q_w^{out}		0	0

In pores containing bulk oil and water films (Table 5, column b), water and oil reside side by side and any trapped oil will not affect the mobility of the water. In the configuration shown in Table 5 column c, however, both bulk water and oil will stop flowing if oil becomes trapped, although water can continue to flow through films if connected to the outlet.

Furthermore, in the more complicated cases with distributed pore shapes and/or contact angles, it is possible that one element with a wetting film will find that none of its downstream neighbours are able to accommodate corner water, i.e. the water film becomes trapped.

It can be seen in Table 5 that in pores with bulk menisci and mobile bulk oil, the configuration itself guarantees a positive water flow gradient. In pores without bulk menisci, however, special treatment is sometimes required. In water imbibition, it is generally assumed that the upstream water supply into a node is no smaller than the downstream demand, *i.e.* that the water flow gradient in each junction is non-negative along the flow direction. However, in some particular cases, due to the surrounding fluid configurations, the flow direction in some pores may reverse, which may lead to a negative water flow difference. In this scenario, the upstream water is not sufficient to maintain the water volume in downstream pores, let alone increase it. In such cases, the model will allow the downstream film to shrink in order to conserve mass. Furthermore, for pores with retreating bulk menisci, the wetting films are also allowed to shrink using a technique introduced below.

Now, at a junction, the total water influx and efflux can be written as:

$$Q_{tot}^{in} = \sum_{upstream} \left| q_w^{out} \right| \qquad \qquad 26$$

and

$$Q_{tot}^{out} = \sum_{downstream} \left| q_w^{in} \right|. \qquad \qquad 27$$

Thus, the volumetric water change at the node, denoted as ΔQ is:

$$\Delta Q = Q_{tot}^{in} - Q_{tot}^{out}. \qquad \qquad 28$$

Based on the potential alteration of water films, downstream pores can be classified into 3 groups. *Group A:* pores containing swelling films – if both the bulk oil and water films are not trapped; *Group B:* pores containing shrinking films – if the wetting films are not trapped, regardless of the mobility of bulk oil; and *Group C:* pores without mobile water films - only single phase (bulk water or bulk oil) can flow into this group of pores.

For each configuration type downstream from a node, water demands can be defined as follows:

Group A:

$$Q_{tot}^{out-(a)} = \sum_{\substack{downstream \\ group(a)}} \left| q_w^{in} \right| \qquad\qquad 29$$

Group B:

$$Q_{tot}^{out-(b)} = \sum_{\substack{downstream \\ group(b)}} \left| q_w^{in} \right| \qquad\qquad 30$$

Group C:

$$Q_{tot}^{out-(c)} = \sum_{\substack{downstream \\ group(c)}} \left| q_w^{in} \right| \qquad\qquad 31$$

The algorithm for distributing water downstream from a node is described below:

(1) If $\Delta Q > 0$, the excess water provided by the upstream pores can be used to swell the water films present in downstream *Group A* pores:

$$q_{w-new}^{in} = q_w^{in} + \Delta Q \cdot \frac{q_w^{in}}{Q_{tot}^{out-(a)}} \qquad\qquad 32$$

(2) However, if the total water influx is not sufficient to feed the downstream pores ($\Delta Q < 0$), but *is* large enough to maintain the water influxes of *Group C* pores ($Q_{tot}^{in} \geq Q_{tot}^{out-(c)}$), then the mass balance can be maintained through shrinking the wetting film in *Group B* pores:

$$q_{w-new}^{in} = q_w^{in} + \Delta Q \cdot \frac{q_w^{in}}{Q_{tot}^{out-(b)}} \qquad\qquad 33$$

Note here that $\Delta Q < 0$, hence the reassigned water influxes are smaller than their corresponding water efflux and film shrinking occurs.

(3) In the very rare case when the total water influx in the node is too low to maintain the required water influxes of *Group C* pores ($Q_{tot}^{in} < Q_{tot}^{out-(c)}$), mass cannot be conserved through swelling or shrinking the film and so the conductance of *all* downstream water pores must be reduced to compensate for this following:

$$g_w = g_w \cdot \frac{Q_{tot}^{in}}{Q_{tot}^{out}} \qquad 34$$

Then the pressure field and local flows of the entire system are updated, and the above calculations repeated. Note that Equation 34 is a temporary solution dealing with a highly rare case, which only affects the adjacent pores (at most 4 pores in 2D model and 6 pores in 3D model) at a particular time step. In practice, we found that it made no difference to the resulting behaviour and include Equation 34 for completeness and transparency. This restriction could be relaxed by using a modified pressure solver.

Note that after redistributing the water influx to eligible downstream pores, we will have $Q_{tot-new}^{out} = \sum_{downstream} |q_{w-new}^{in}| = Q_{tot}^{in}$, *i.e.* the water flow regains its balance at each node. To summarise, the above process effectively moves the water-flow imbalance from the node to the downstream pores and uses this pore-level gradient to update the downstream wetting films.

f) Time step

The time step is chosen to conserve mass and guarantee that at most *one* pore can become completely filled by invading water in a single time step (or, in the case of a shrinking wetting film, the *AM*s can at most retreat to the corners of the pore). Also, note that the formulae for calculating the water conductances differ between pores with a thin film and a thick film after *AM*s merge. Thus, over the course of a single time step, *AM*s in at most one pore can swell or shrink to the coalescence point ($A_w = A - A_o^{snap-off}$). Referring to the possible fluid configurations, the associated time step choices are summarised in Figure 4:

23

Figure 4 Time step associating with particular configuration changes. Blue represents water and red represents oil. Blue arrows indicate swelling films and/or advancing bulk menisci; red arrows represent shrinking films; black dashed arrow represents immobile films caused by trapped oil or water-filled pores.

Advancing bulk menisci and film swelling coexist in pores with bulk water and wetting film, and so Δt_4 is determined by the first event that occurs in this pore. Hence the ΔV_w^* term is given by

$$\Delta V_w^* = \min(V_o, \frac{(A_o - A_{critical}) \cdot (l - d)}{\lambda}), \qquad\qquad 35$$

and the final choice of time step is given by:

$$\Delta t = \min(\Delta t_1, \Delta t_2, \Delta t_3, \Delta t_4, \Delta t_5, \Delta t_6, \Delta t_7). \qquad\qquad 36$$

Considering all of the above events in the calculation of the time step, Δt may be very small, especially in low-rate simulations that include all film behaviours – it may take several time steps for one single pore to be fully filled. Consequently, the simulation time will be prolonged and, with larger networks, this efficiency issue will become more serious. However, we took this rather conservative view here to ensure the model would work reliably. We may relax this algorithm in a future improved model to increase the simulation efficiency and model's ability to simulate larger networks. A two-phase pressure solution approach may help in this respect.

g) Phase Trapping

Bulk oil is considered as being trapped when it becomes disconnected from the outlet and so water encountering trapped oil can only flow around it through water films - a process which involves no oil displacement.

Whilst a topology-based trapping protocol (such as that proposed by Hoshen and Kopelman (1976)) is fine for steady-state models, it is no longer adequate here, since the *local flow direction* will also have an impact on oil trapping. For the schematic example shown in Figure 5, the circled pores containing oil are all topologically connected to the outlet and would be free to leave the system under the assumptions of topological trapping. However, given their flow directions, they are actually trapped due to the lack of an available *downstream* path. Because we are dealing with a dynamic simulation here, a new trapping algorithm is required that takes into account this important facet of the displacement.
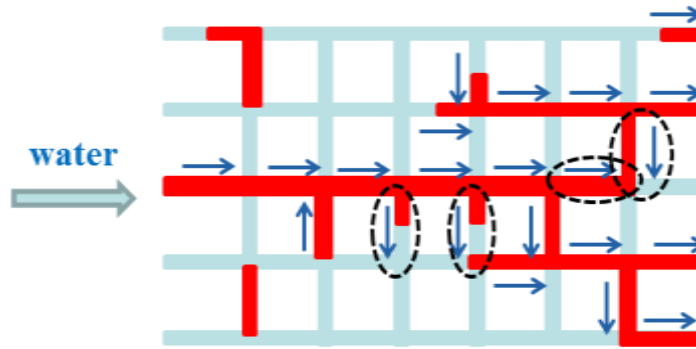
Figure 5 Illustration of the clustering algorithm.

Red is oil and blue is water. Arrows indicate the flow direction.

A *Depth-First Search* (*DFS*) backtracking algorithm has been applied to find all the oil-trapped pores based on both topology and local flow direction. First, the algorithm labels all the oil-filled pores as being trapped and then, starting from the outlet oil-occupied pores, the search will go as far as possible against the flow direction to identify (and "un-trap") all upstream oil-occupied pores. The model searches each upstream neighbour in a specific order remembering the elements it has already explored and it will not visit these again. A backtracking point is identified when the search reaches either an inlet pore, a partially-filled pore, or a point where all the upstream neighbours have already been visited and managed.

The work flow, with all the details of *DFS x-direction* is shown in Figure 6. The algorithms for y-pores and z-pores are essentially the same as that used for x-pores, only with a little modification to identify the upstream neighbours.
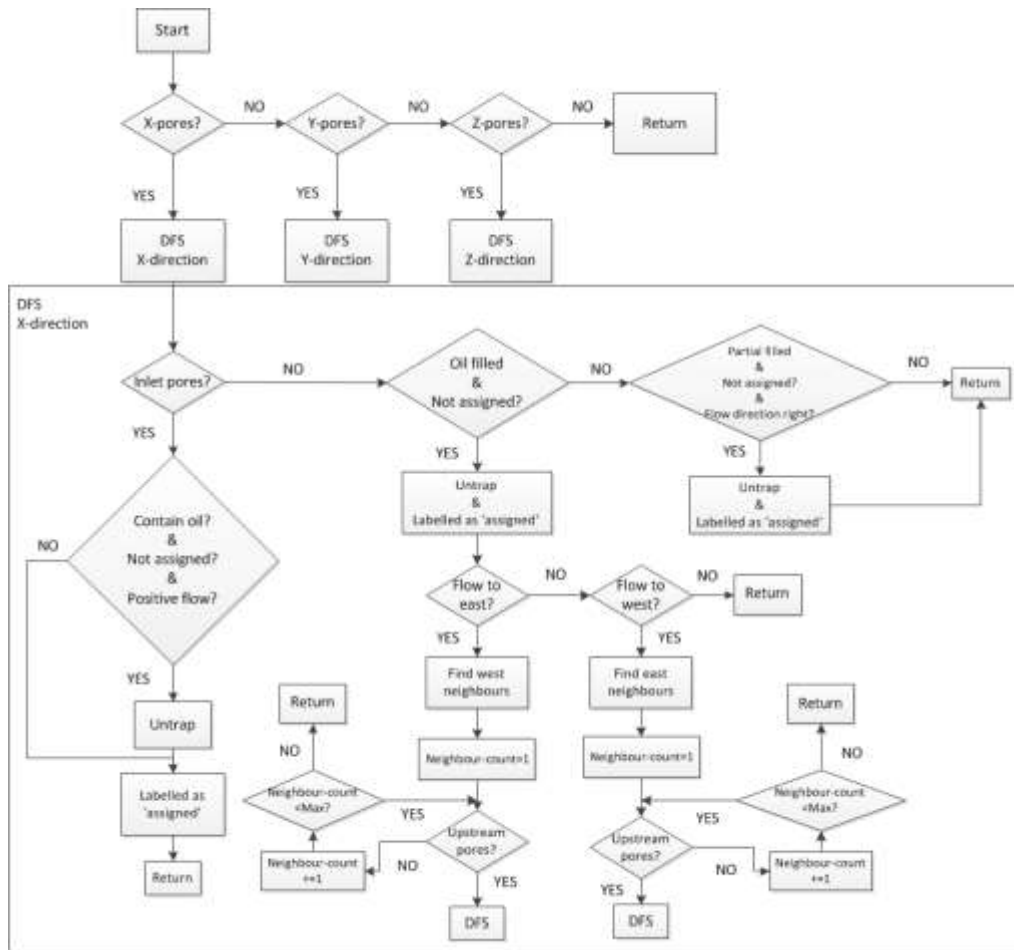
Figure 6 Work flow of the Depth First Search (DFS) algorithm

Topology-based trapping algorithms that do not account for flow direction will not only underestimate the extent of trapped oil but will also lead to mass conservation errors and affect water configurations.

A similar trapping algorithm is also applied to the wetting films, since in a system with distributed contact angle and/or pore shapes, it is possible that some pore elements with wetting films find that all of their *downstream* neighbours have no ability to accommodate corner water. In such cases, their films become trapped and water efflux is cut off. Furthermore, if for a particular pore, all its downstream neighbouring elements contain trapped films, the film within this pore will also be trapped.

III.   DETAILED ANALYSIS OF LOCAL SWITCH AND NUMERICAL RESULTS

a) Detailed analysis of local switch (λ)

Two phase *drainage* processes in porous media have been characterised by two dimensionless numbers: namely, the ***capillary number*** C_a, and ***viscosity ratio*** *M* (<u>Lenormand et al. (1990)</u>).   Whilst these groups also apply in imbibition, we will demonstrate that some *additional* quantities or control parameters also arise, as discussed below.   The capillary number, C_a, represents the competition between capillary and viscous forces and one form of this quantity, applied in this work, is:

$$C_a = \frac{\mu_w Q}{\sigma_{ow} \Sigma} \qquad\qquad 37$$

where μ_w ($\mathrm{N \cdot s/m^2}$) is the advancing phase (water) viscosity, Q ($\mathrm{m^3/s}$) is the volumetric flow rate, σ ($\mathrm{N/m}$) is the interfacial tension, and Σ ($\mathrm{m^2}$) is the cross sectional area of the inlet face of the medium; in this work , we approximate Σ as $n_y \cdot 2r_{mean} \cdot l$ in 2D networks and $n_y \cdot n_z \cdot l^2$ in 3D networks.

The **viscosity ratio**, *M*, is defined as the ratio of defending (oil) phase viscosity, μ_o, to advancing (water) phase viscosity, μ_w, as follows:

$$M = \frac{\mu_o}{\mu_w} \qquad\qquad 38$$

In addition to the quantities C_a and *M*, we introduce the local switch parameter, $\lambda = P_c/(P_c + \Delta P)$, to simulate the local competition between viscous and capillary forces (Figure 7) and consequently the balance between the two main pore filling mechanisms: piston-like displacement and snap-off. It should be stressed that λ is *not* input, it is calculated locally during the simulation. A further important parameter in imbibition is the *wettability* of the porous medium expressed through the oil/water contact angle (i.e. θ_{ow} and its distribution), which also profoundly affects the flow regimes which emerge in imbibition; this is also included in our model.
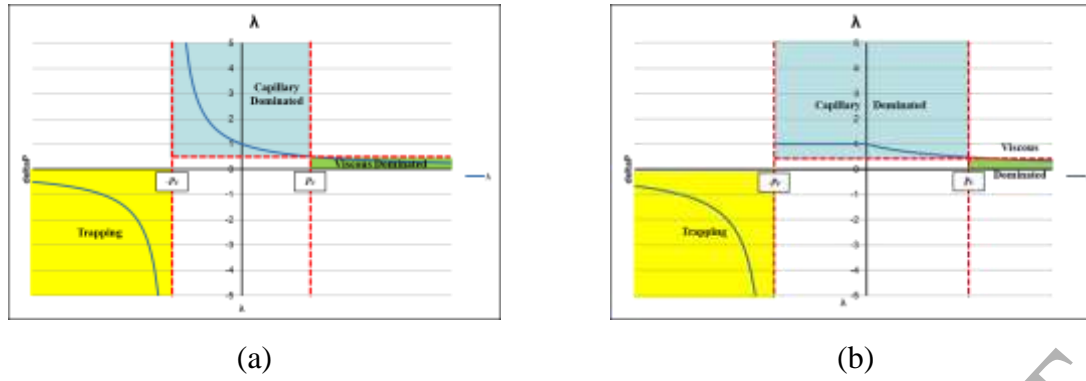
28

(a)   (b)

Figure 7 Schematics showing the dominant displacement mechanism within a pore as a function of the local switch parameter (λ) and pressure gradient (ΔP). (a) blue curves resulting directly from Equation 18, (b) modified curves after invoking the condition that λ<1.0. Note that the vertical dashed lines correspond to values of ΔP equal to $\pm \ P_c$ equal to the vertical dashed lines correspondingly.

With reference to Figure 7 (a), note that, with the help of capillary pressure, the viscous pressure gradient from the water-filled end of a pore to its oil-filled end does not need to be positive to have a positive flow rate. In fact, so long as $-P_c < \Delta P < P_c$, the pore will undergo capillary dominated displacement, with P_c having progressively less impact as the viscous pressure drop across the pore increases. If $\Delta P > P_c$, viscous forces begin to dominate the displacement, whilst for viscous gradients satisfying $\Delta P < -P_c$, no displacement occurs (as the flow would otherwise be counter-current).

For pores with a bulk meniscus, the local flow rate is given by $q = g \cdot (\Delta P + P_c)$, thus the representation of this switching parameter can also be written as:

$$\lambda = \frac{P_c}{q} \cdot g .$$
                                                                                    39

However, another consequence of the switching parameter must also be taken into account: the value of λ is used to determine the relative partition of inflowing water into advancing bulk water and swelling water films (as per Equation 20), and so the maximum value of the switching parameter should be restricted to unity (Figure 7 (b)).

To explore the precise relationship between λ and other parameters of interest in the system, we first consider *a single pore* in which water is injected at a constant rate q at one end and the other end functions as an outlet. We will also assume that there is no initial water in this

29

water-wet pore, and that the cross section is a scalene triangle. The representations of P_c is given by Equation 9, and the total conductance of this triangular pore is

$$g = \frac{3r^2 A}{20\bar{\mu}l} \qquad\qquad 40$$

where $\bar{\mu}$ is the average viscosity of the system governed by the volume ratio of the phases and particular configuration of each phase. As the displacement progresses, the value of $\bar{\mu}$ will alter accordingly. For simplicity, the analysis of λ below will focus on the initial value of λ (noted as λ^*), when the bulk meniscus just enters this pore, $\bar{\mu} = \mu_o$ (thus, we can eliminate the effect of particular fluid configurations and only consider the influence of the set parameters on the local switch). The expression for λ^* then can be expanded as:

$$\lambda^* = \frac{3F_d^{piston-like} \cdot \sum_{i=1}^{3}\frac{1}{\tan\beta_i}}{20} \cdot \frac{\sigma_{ow} \cdot r^3}{\mu_o q l} \qquad\qquad 41$$

Equation 41 now defines the relationship between the switch value and *all* the pore-scale parameters of importance: viz. flow rate, pore size (inscribed radius and lengths), contact angle, pore geometry (corner angles) and interfacial tension. Simulation results from a parametric sensitivity study of this equation can be found in Li (2016), and will also be reported in a future paper.

If we denote the pore-scale aspect ratio to be the ratio of inscribed radius to pore-length

$$R_{asp} = \frac{r}{l}, \qquad\qquad 42$$

and consider pore cross-sectional area, capillary number, and viscosity ratio (Equation 1, Equation 37, and Equation 38 respectively), then the above equation for the λ switch in Equation 40 can be expressed in terms of wettability, capillary number, viscosity ratio and aspect ratio, as follows:

$$\lambda^* = \frac{3F_d^{piston-like}}{20} \cdot \frac{R_{asp}}{M \cdot C_a}. \qquad\qquad 43$$

30

b) **Influence of the capillary/viscous force balance (λ) during network flow**

In this model, the water viscosity will be held fixed at $1.0e^{-3} \, \mathrm{N \cdot s/m^2}$; (i.e. 1mPa.s) and, by altering the oil viscosity, we can simulate water injection experiments in "light oil" (lower μ_o) and "heavy oil" (higher μ_o) systems.

Unless otherwise indicated, the parameters of importance in this model will be assigned the default values listed in Table 6. *Also, initially, there is no water in the system*, *i.e.* all pores start with volume-less water films. Each simulation continues until all outlet pores become filled with water (at which point no further displacement of oil is possible).

Table 6 List of default parameters used in this study

Parameter	Default value	Unit
Network size	100*50 (2D) 20*20*20 (3D)	Node
Coordination number (Z)	4 (2D), 6 (3D)	-
Pore size (uniform) (r)	1-50	μm
Distortion number[1]	0.3	-
Average pore length (l)	333	μm
Pore half angles (β_i)	30,30,30	degree
Wettability class	Water wet	-
Water/oil contact angle (θ_{ow})[2]	0	degree
Interfacial tension (σ)	40.0	mN/m
Initial water saturation (S_{wi})	0.0	-
The resistance factor of solid (C_w)[3]	100	-

Notes 1. The distortion number is a method of taking a regular 2D or 3D lattice and making it more irregular (see McDougall (1994));

2. The dynamic model includes the contact angle (θ_{ow}) as a parameter.

3. The resistance factor of the solid (C_w) – see Table 4.

By default, the dynamic pore network model automatically calculates the capillary/viscous switch (λ) based on the local pressure drop and capillary entry pressure. However, this model also allows us to *predefine* the value of the switch, enabling us to *force* the water/oil displacement to be purely piston-like (λ = 0) or purely snap-off (λ = 1), regardless of the

31

capillary number. This is a useful construct that allows us to identify the specific influence of different forces in complex displacement cases more easily.

For illustrative purposes, the influence of the switch parameter (λ) is demonstrated under conditions of unfavourable viscosity ratio (*M=10.0*). Figure 8 (a), (c), (e) show snapshots of displacements whilst Figure 8 (b), (d), (f) illustrate the corresponding local water saturation maps. These figures are shown when an identical amount of water (0.192 PV) has been injected into each network and the distinction between these sets of figures (throughout this paper) is as follows: Figure 8 (a), (c), (e) show the pores filled by different phases, where red represents completely water-filled pores and white represents the pores that are oil-filled or partially oil-filled (with or without a wetting film); this segments the phase occupancies in a "binary" manner. In contrast, Figure 8 (b), (d), (f) represent the local water saturation (S_w), the colour changes denote the increasing water saturation in the order: white (lowest S_w) light blue, light purple, dark purple, to dark blue (highest S_w); the black region corresponds to water-free (i.e. completely oil filled) pores.

In all three cases, we see that the dark blue (high S_w) clusters in the saturation plots (Figure 8 (b), (d), (f)) corresponds closely to the red clusters in the phase plots (Figure 8 (a), (c), (e)). Thus, the combination of the *two* types of fluid distributions of the *same* data in Figure 8 (i.e. (a), (c), (e) and (b), (d), (f)) show all the subtleties of the flow regimes which occur in imbibition (especially of those related to wetting films). This is distinct from two phase *drainage* displacements characterised by piston-like displacement, where the simple binary occupancies (as in (a), (c), (e)) describe the displacement quite adequately. Figure 8 (a) and Figure 8 (b) show the results when λ=0.0 (only piston-like displacement is allowed); (c) and (d) are the results corresponding to the automatic switch (λ calculated based on the local balance of forces), whilst (e) and (f) show the results of the system where snap-off is forced to be the primary filling mechanism (λ=1.0).

In Figure 8 (a) and (b) only piston-like pore scale displacements are allowed for imbibition (λ = 0.0), it is essentially modelling imbibition as a direct "inversion" of drainage. The results in Figure 8 (c) and (d) show that when either mechanism is allowed in imbibition according the local balance of forces (λ calculated automatically), then the remnant underlying fingering patterns of the piston-like displacement is still visible but very significant "capillary fringing" is now observed. For this specific injection rate (*Q=1.0e^{-6}m^3/s, C_a=2.94e^{-2}*), the initial value of the automatic switch λ is close to 0.0 throughout the system and so bulk

piston-like advancement is more dominated during the fully dynamic flood. However, during imbibition, local switch will keep increase as clearly shown in Figure 9, and it has a very significant effect on the detailed water (and oil) distribution in the network; this is seen by comparing the fluid distributions in Figure 8 (b) and Figure 8 (d).

When the value of the switch is artificially set to λ=1.0, more film swelling and snap-off occurs and the water configuration changes from continuous bulk paths to more scattered clusters (Figure 8 (a)-(c)-(e)). In the simulations where λ is calculated automatically (Figure 8 (c), (d)), the fluid distributions are distinctly "intermediate" between the two extremes that allow just one mechanism or the other.
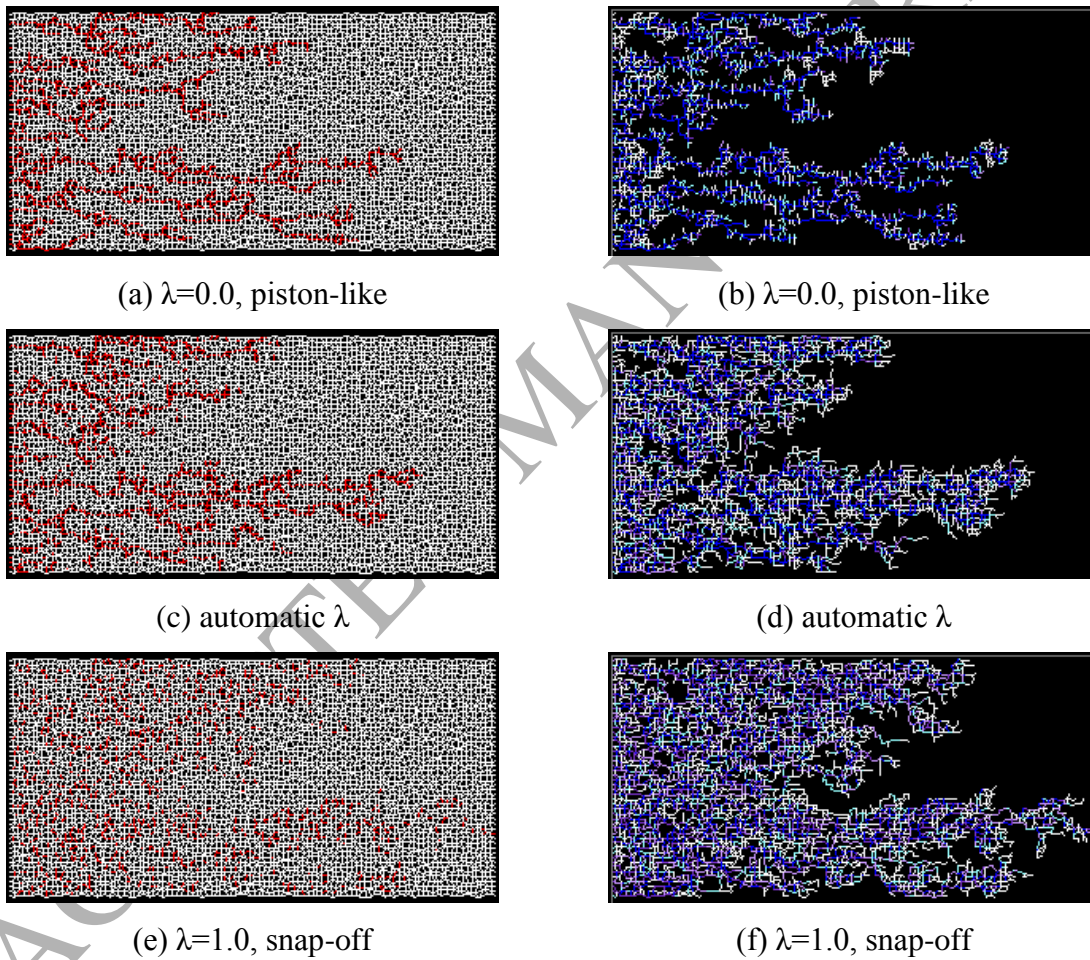

(a) λ=0.0, piston-like

(b) λ=0.0, piston-like

(c) automatic λ

(d) automatic λ

(e) λ=1.0, snap-off

(f) λ=1.0, snap-off

Figure 8 The influence of the switch, λ, on an imbibition simulation with *Q=1.0e⁻⁶m³/s*, *Ca=2.94e⁻²*, *M=10.0*. The figures are shown when an identical amount of water (0.192 PV) has been injected into each network. All network input data in Table 6.

As discussed above, in the calculation of λ, Equation 40 is used to calculate the local conductance. More specifically, when *M=10.0*, $\bar{\mu}$ will keep decreasing during imbibition due

to the accumulation of less viscous water. Consequently, λ will continuously go up given the water flow rate remains constant (Equation 39). Note this analysis is applied on a single pore, while in network, due to the influence of surrounding conditions, alteration of local λ is more difficult to predict. Our model, however, successfully monitor the change of local λ and confirm the general upward trend of local λ. Based on the number of selected pores (a quantity that can be predefined), the model can randomly choose several pores and record the values of their switch at each time step *if* these pores contain bulk menisci and mobile oil. Each curve in Figure 9 tracks the switch changing of one particular pore, and the x-axis represents the number of time steps.
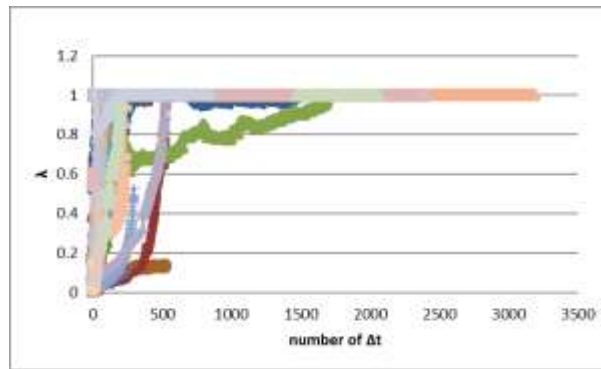

Figure 9 Local Switch evolution in simulation with *Q=1.0e^{-6}m^3/s*, *Ca=2.94e^{-2}*, *M=10.0*. Each curve represents the value of a switch in a particular pore at each time step, the x-axis is the number of time steps.

Furthermore, the local distribution of the pore-scale switch during the displacement can be visualized. Since the network model only calculates λ in a pore when it has both the bulk menisci and *mobile* oil, the map of local switch values at any given time actually outlines the bulk water front. Figure 10 illustrates the local λ distribution at the same moment as Figure 8 (c) and (d). As λ increases, the colour will change in the order of white (λ=0.0), light blue, light purple, dark purple, to yellow (λ=1.0).
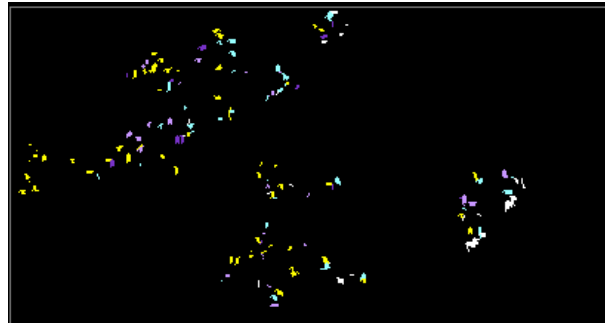
Figure 10 Switch map in simulation with *Q=1.0e⁻⁶m³/s*, *Ca=2.94e⁻²*, *M=10.0*. As λ increases, the colour will change in the order of white (λ =0.0), light blue, light purple, dark purple, to yellow (λ =1.0). The figure is shown when 0.192 PV of water has been injected into the network, like Figure 8 (c) and (d).

Figure 11 shows the 3D results in which different switch (λ) assumptions are made in the intermediate-rate model (*Q=1.0e⁻⁵m³/s*) with unfavourable viscosity ratio (*M=10.0*). Similar as Figure 8, Figure 11 (a), (c), (e) show snapshots of displacements and (b), (d), (f) illustrate the corresponding local water saturation maps. For this injection rate, water should displace oil through both bulk advancement and film swelling mechanisms: starting value of λ in each pore is generally 0.0, and as less viscous water displacing oil during water imbibition, λ will gradually increase to 1.0 (as illustrated in Figure 12). However, if we set λ =0.0, then film swelling is completely suppressed and, likewise, when we make λ =1.0, only snap-off occurs throughout the network. Regardless of the value of the switch, the capillary number is constant at *5.64e⁻³*. However, it is clear from the 3D network displacement patterns in Figure 12 that the flows are very different and we would expect that this ***must*** have some influence of the resulting relative permeability curves (Figure 14).
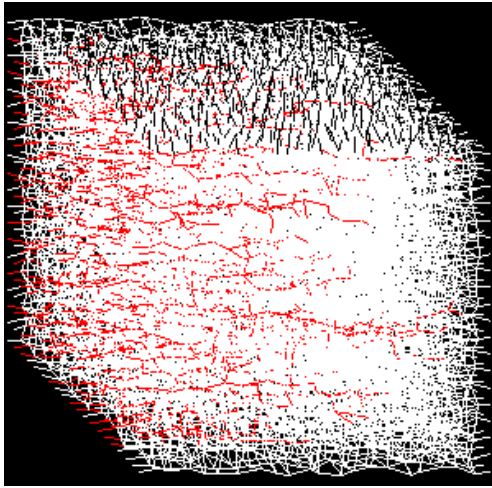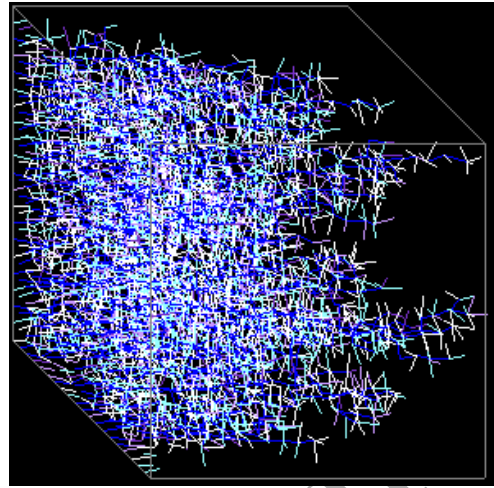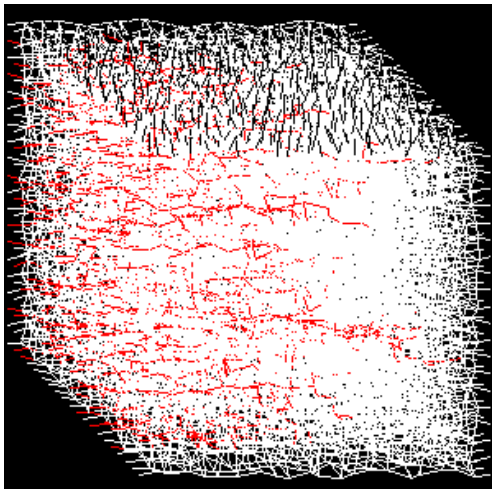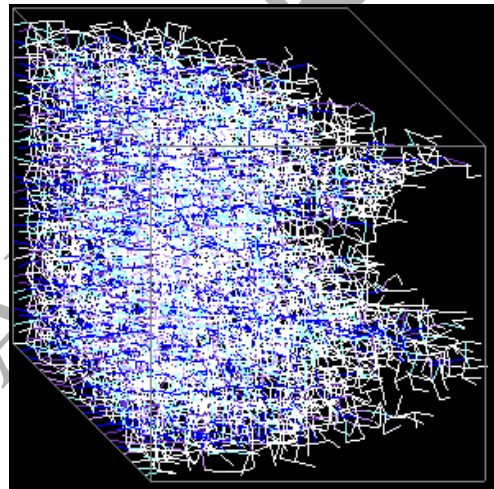
35

(a) λ=0.0, piston-like

(b) λ=0.0, piston-like

(c) automatic λ

(d) automatic λ
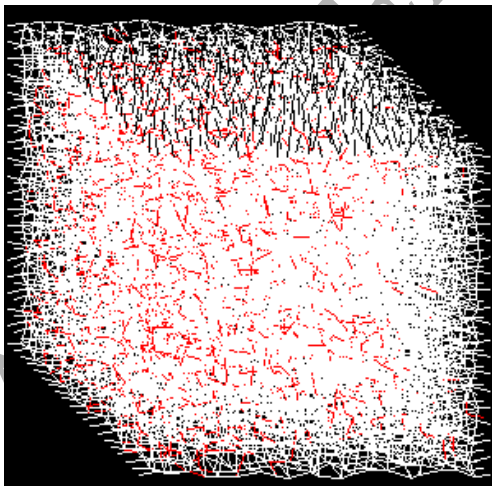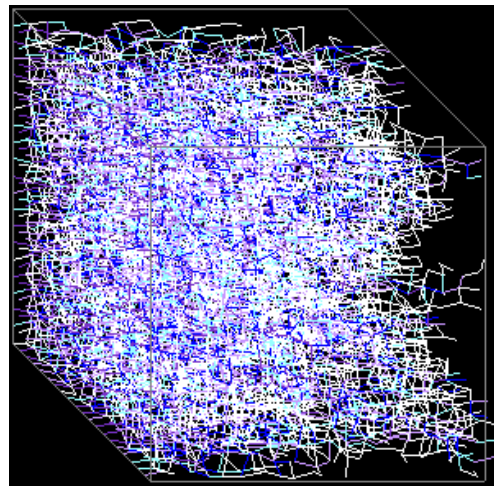
(e) λ=1.0, snap-off

(f) λ=1.0, snap-off

Figure 11 The influence of the switch, λ, on an imbibition simulation with $Q=1.0e^{-5}m^3/s$, $Ca=5.64e^{-3}$, $M=10.0$. The figures are shown when an identical amount of water (0.162 PV) has been injected into each network. All network input data in Table 6.
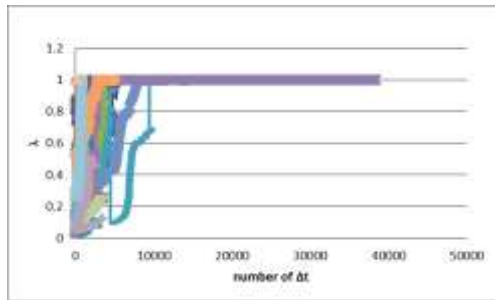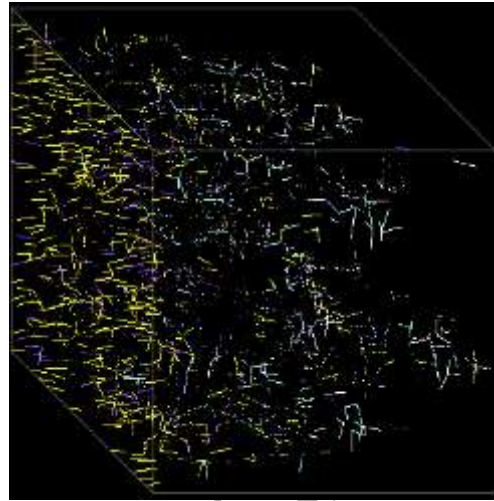
<table>
<tr><td>(a) λ evolution curve</td><td>(b) λ distribution map</td></tr>
</table>

Figure 12 Local Switch evolution and distribution in simulation with **$Q=1.0e^{-5}m^3/s$**, **$Ca=5.64e^{-3}$**, **$M=10.0$**. In (a) each curve represents the value of switch in a particular pore at each time step, the x-axis is the number of time steps. The figure (b) is shown when 0.162 PV of water has been injected into the network, like Figure 11 (c) and (d).

In these constant flow rate simulations with unfavourable viscosity ratio (*M=10.0*), the pressure drop decreases more over time to counteract the growing global conductance (due to the decreasing global average viscosity) and maintain the flow rate. Compared to piston-like displacement, snap-off is more likely to cause oil trapping and reduce the global conductance, which has the opposing effect of the less viscous invading water. Therefore, although with identical injection rate, the global pressure drops are quite different, as shown in Figure 13 (a), to be specific, smallest pressure drop reduction is observed in the purely snap-off case. Therefore, we immediately may suspect that the dynamic balance between capillary and viscous forces (i.e. λ) should lead to different USS relative permeability curves (Figure 14) because of this change in total mobility in the system.

From bulk model to automatic- λ model to film model, increasing levels of film-swelling and snap-off will lead to more and more severe oil-trapping, which explains the earlier water breakthrough and worse oil recovery (Figure 13 (b)) in the corresponding cases with larger value of λ.

37

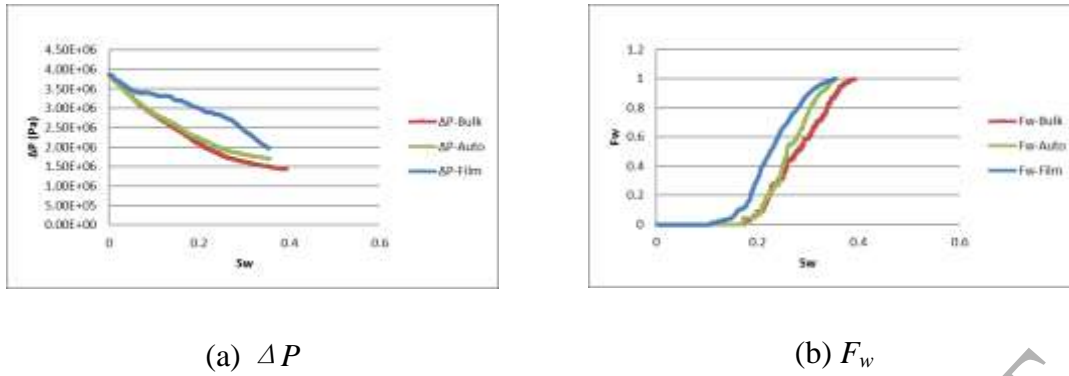(a) ΔP (b) F_w

Figure 13 Global pressure drops and water fractional flow from simulations carried out under various switch assumptions, $Q=1.0e^{-5}m^3/s$, $Ca=5.64e^{-3}$, $M=10.0$.

Based on Buckley-Leverett theory, the model can be used to obtain the relative permeability curves (Figure 14) using water fractional flow (Figure 13 (b)) and global pressure drop data (Figure 13 (a)). Figure 14 verifies that more film swelling and snap-off will cause more oil-trapping and reduce the value of k_{ro}.
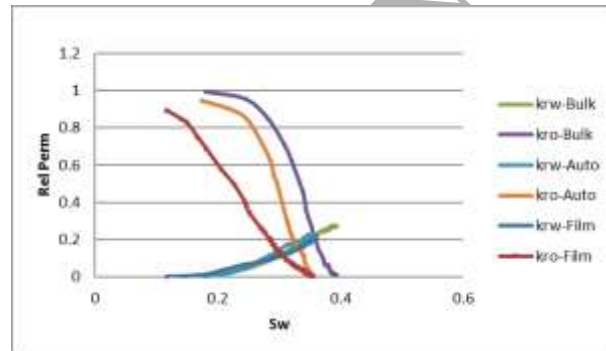
Figure 14 Relative permeability curves from simulations carried out under various switch assumptions, $Q=1.0e^{-5}m^3/s$, $Ca=5.64e^{-3}$, $M=10.0$.

c) Influence of flow rate (Q) and viscosity ratio (M)

If we change the injection rate in our simulator, then the pressure drop across the whole system (as well as across each pore) will alter accordingly. This means that the *local* switch (λ) will of course be affected by the *global* flow rate. In a high rate case with a large pressure drop, viscous forces will largely control the displacement and relatively small λ values (associating with piston-like displacement) will dominate locally. Conversely, low-rate, capillary-dominated floods will be characterised by larger switch values which, under these circumstances, lead to a better water supply to feed downstream swelling films. The overall

complexity of the imbibition process is in large measure a result of the competing influences just described.

Figure 15 shows the fluid configurations ((1), (4), (7), (10)), local water saturation ((2), (5), (8), (11)), and local λ distribution ((3), (6), (9), (12)), from fully dynamic imbibition simulations (λ calculated automatically) over a wide range of injection rates (capillary numbers, $C_a = 2.94e^{-1} - 2.94e^{-4}$). In the high rate flood (Figure 15, 1st row), most of the waterflood is seen to occur through the advancement of bulk menisci; whereas the low injection rate case (Figure 15, 4th row) is mainly characterised by the swelling of wetting films and snap-off; in simulations at intermediate injection rates (Figure 15, 2nd and 3rd row), both mechanisms co-exist and, as flow rate decreases, growing numbers of disconnected water-filled clusters caused by snap-off are observed. The transition between the various regimes is clear with, (i) the highest rate viscous dominated case showing viscous fingering, but with *some* observable "capillary fringing", followed by (ii) a "mixed" regime showing the capillary dissipation of the remnant viscous fingering, through to (iii) a clear capillary dominated regime, where viscous effects *appear* to be absent (note that these viscous effects are not *completely* absent; they still have an underlying influence on the final fluid distributions; this will be evident below where we show similar comparisons of $M = 10.0$ and $M = 1.0$ cases).

(1) $C_a=2.94e^{-1}$ (2) $C_a=2.94e^{-1}$, S_w (3) $C_a=2.94e^{-1}$, λ

(4) $C_a=2.94e^{-2}$ (5) $C_a=2.94e^{-2}$, S_w (6) $C_a=2.94e^{-2}$, λ

(7) $C_a=2.94e^{-3}$ (8) $C_a=2.94e^{-3}$, S_w (9) $C_a=2.94e^{-3}$, λ

(10) $C_a=2.94e^{-4}$ (11) $C_a=2.94e^{-4}$, S_w (12) $C_a=2.94e^{-4}$, λ
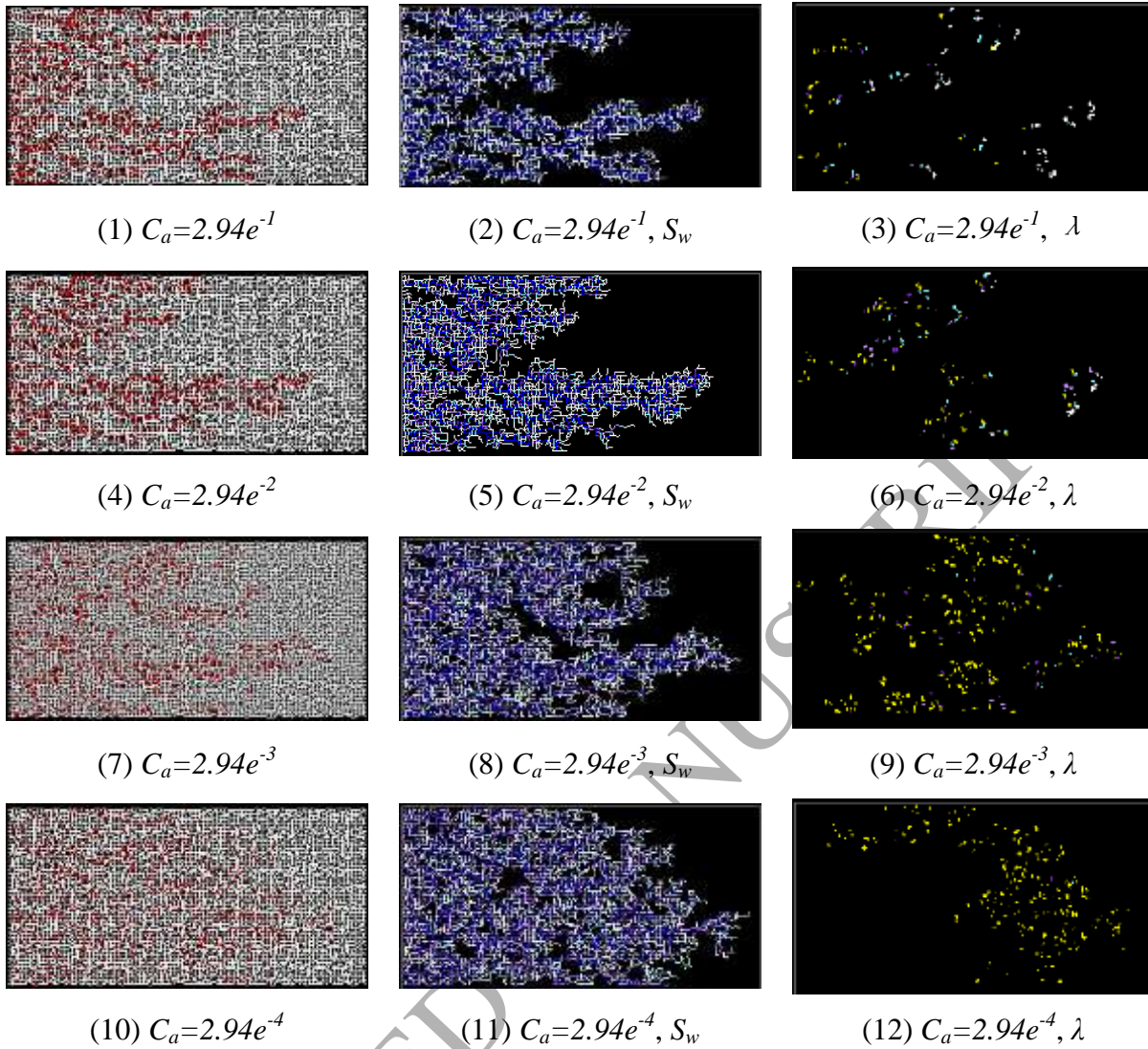
Figure 15 Fluid configurations, local water saturation, and local λ distribution in simulations with **M=10.0** and various **flow rates**. The figures are shown when an identical amount of water (0.192 PV) has been injected into each network. All network input data in Table 6.

The distribution of local switch value is shown in third column of Figure 15 and Figure 16 – in *M=10.0* case, λ in each pore will generally increase to 1.0 as water displaces oil. But water flow rate will affect the initial value of local λ, especially in the lowest-rate case (Figure 16 (d)).

(a) $C_a=2.94e^{-1}$

(b) $C_a=2.94e^{-2}$

(c) $C_a=2.94e^{-3}$

(d) $C_a=2.94e^{-4}$
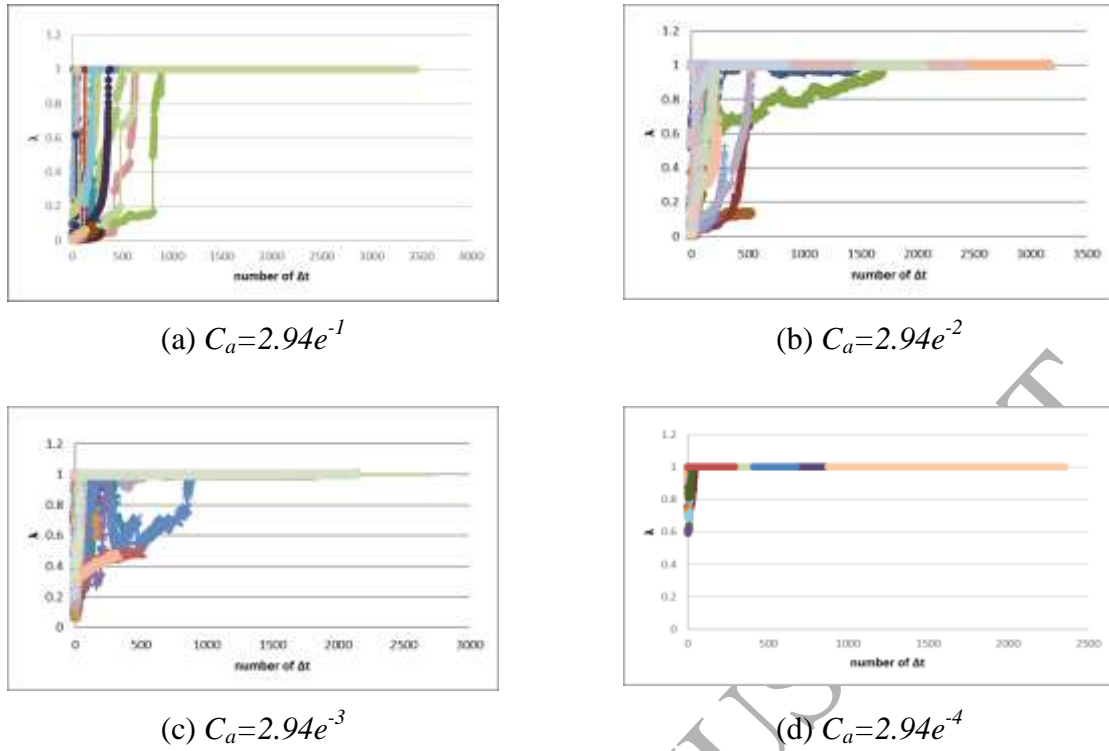
Figure 16 Local Switch evolution in simulation with **M=10.0** and various **flow rates**. Each curve represents the value of switch in a particular pore at each time step, the x-axis is the number of time steps.

Figure 17 shows the effect of mobility ratio, M, for a high rate flood rate ($Q=1.0e^{-5}m^3/s$, $C_a=2.94e^{-1}$) with automatic λ calculation in the base case network (Table 6) for cases with M = 0.1 in Figure 17 (a) and (b), $M = 1$ in Figure 17 (c) and (d), $M = 10$ in Figure 17 (e) and (f). In the $M = 0.1$ viscous over-stable case, a very compact water cluster is found with a clear stable frontal structure. In the $M = 1.0$ neutral-stable case, the entire water cluster is much less compact and the frontal structure exhibits a transitional fringe due to the effects of capillarity. In the $M = 10.0$ viscous unstable case, fully developed viscous fingering is observed, although there is still some overlay of capillarity.

41

(1) *M=0.1*

(2) *M=0.1, Sw*

(3) *M=0.1, λ*

(4) *M=1.0*

(5) *M=1.0, Sw*
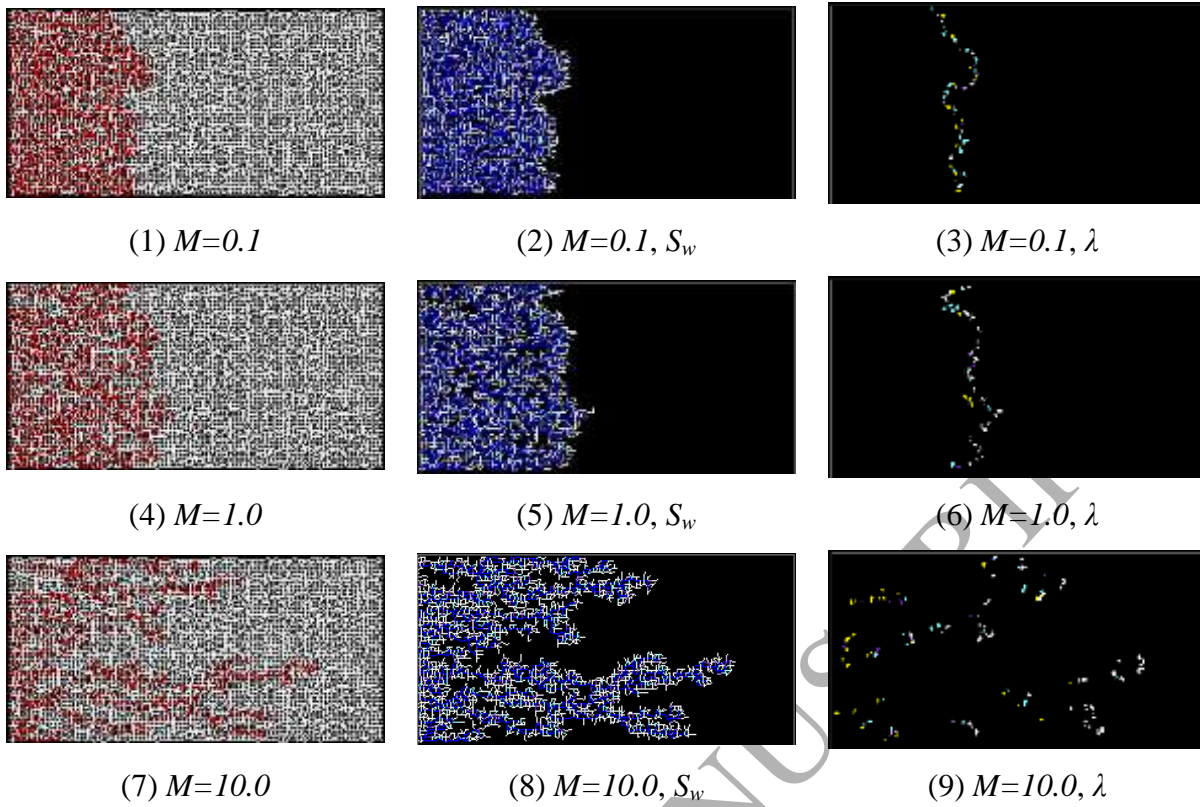

(6) *M=1.0, λ*

(7) *M=10.0*

(8) *M=10.0, Sw*

(9) *M=10.0, λ*

Figure 17 Fluid configurations, local water saturation, and local *λ* distribution in simulations with various viscosity ratios and $Q=1.0e^{-5}m^3/s$, $Ca=2.94e^{-1}$. The figures are shown when an identical amount of water (0.192 PV) has been injected into each network. All network input data in Table 6.

Figure 18 displays local switch evolution in simulation with various viscosity ratios, from which we can study the influence of viscosity ratio on capillary/viscous switch from both initial values and changing tendencies. Very broadly for this flow rate, this initial $λ$ is inversely proportional to the viscosity ratio. And to the opposite of *M=10.0* case, more viscous injected water in *M=0.1* case will cause the $λ$ drop, whilst in the *M* = 1.0 neutral-stable case, values of local *λ* are relatively stable, except the sudden "jump" due to alteration of surrounding fluid configurations.
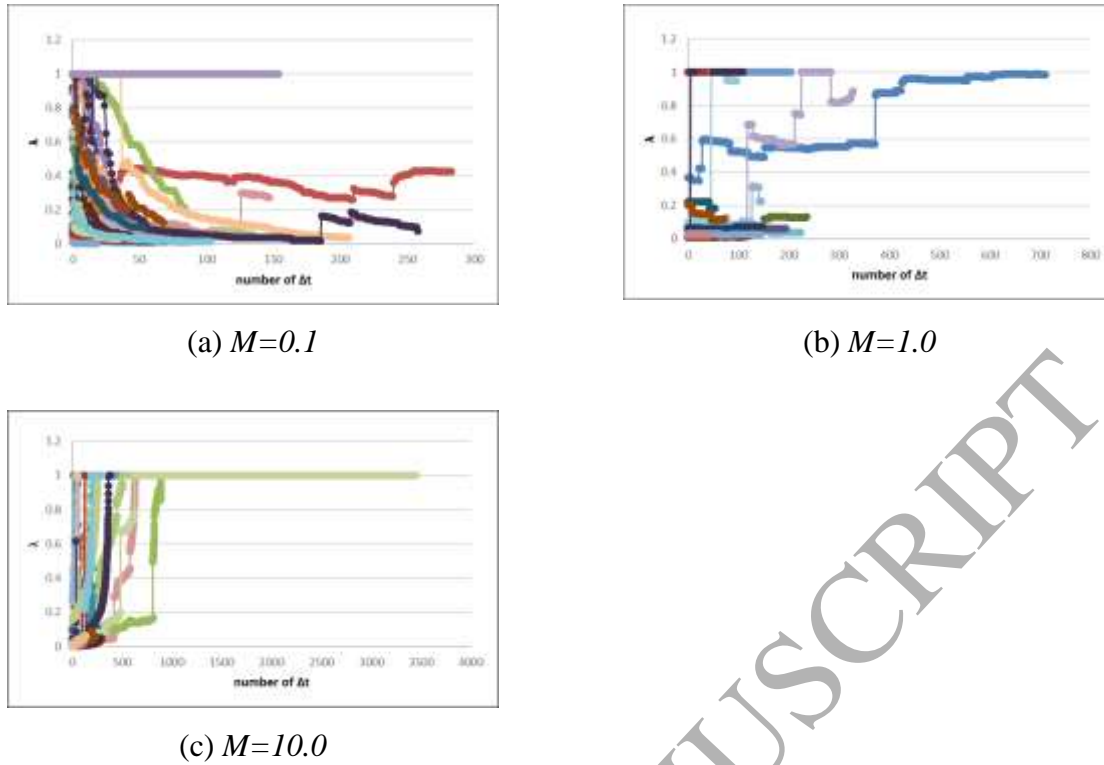
42

(a) *M=0.1*

(b) *M=1.0*

(c) *M=10.0*

Figure 18 Local Switch evolution in simulation with various viscosity ratios and *Q=1.0e^{-5}m^3/s*, *Ca=2.94e^{-1}*. Each curve represents the value of switch in a particular pore at each time step, the x-axis is the number of time steps.

Figure 19 shows *very low rate* ($Q=1.0e^{-8}m^3/s$, $C_a=2.94e^{-4}$) simulations for the dynamic imbibition model (λ automatic) with M = 1.0 and 10.0. It is clear that values of local λ in both cases are close to 1.0, thus capillary forces dominate the displacement *but* the extent of snap-off is still controlled to some degree by the viscosity ratio, *M*. This is in contrast to a corresponding pure capillary dominated drainage process (invasion percolation), where these two flow patterns for M = 1.0 and 10.0 (Figure 19) would be identical. Thus, in low rate imbibition the flow pattern does not collapse to the same fluid distribution even though it is considered to be "capillary dominated"; the effects of viscosity are still present and we describe this as a "deep coupling" between viscous and capillary effects in imbibition. The differences in flow pattern at very low flow rates shown in Figure 19 are due to the different viscosities of the water and oil which lead to the (water) wetting films having a much greater relative mobility in the M = 10.0 case, thus leading to a higher level of film swelling/snap-off, which results in local oil cluster bypassing and trapping, and hence poorer non-wetting phase recovery. This simulation indicates why the microscopic displacement efficiency is lower for higher M cases in water imbibition processes.
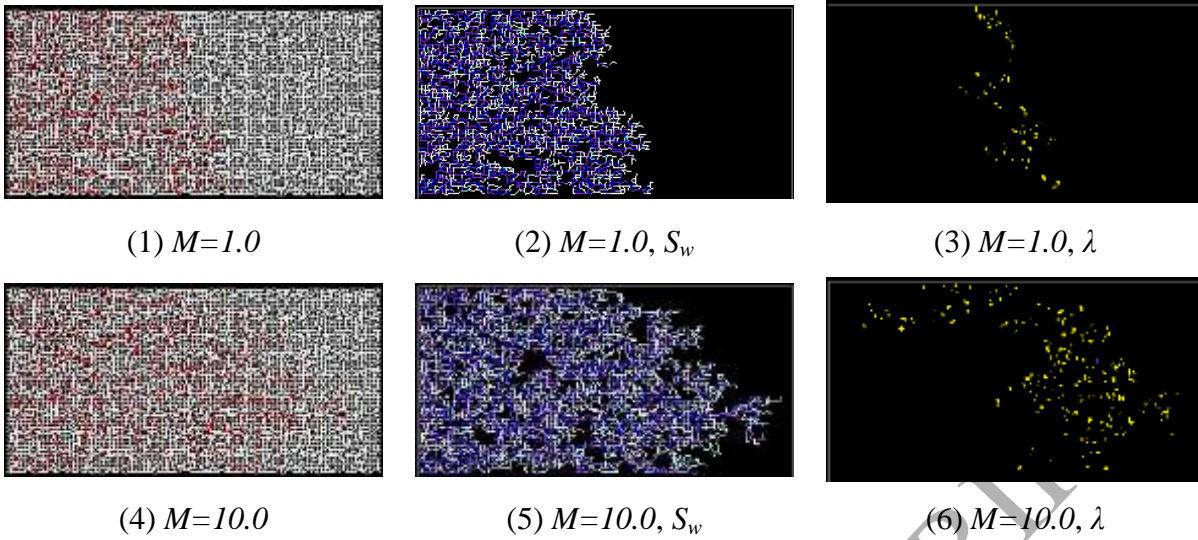
43

(1) *M=1.0*　　　　　　(2) *M=1.0, S$_w$*　　　　　　(3) *M=1.0, λ*

(4) *M=10.0*　　　　　　(5) *M=10.0, S$_w$*　　　　　　(6) *M=10.0, λ*

Figure 19 Fluid configurations, local water saturation, and local *λ* distribution in simulations with various ***viscosity ratios*** and ***Q=1.0e^{-8}m^3/s***, ***C$_a$=2.94e^{-4}***. The figures are shown when an identical amount of water (0.192 PV) has been injected into each network. All network input data in Table 6.
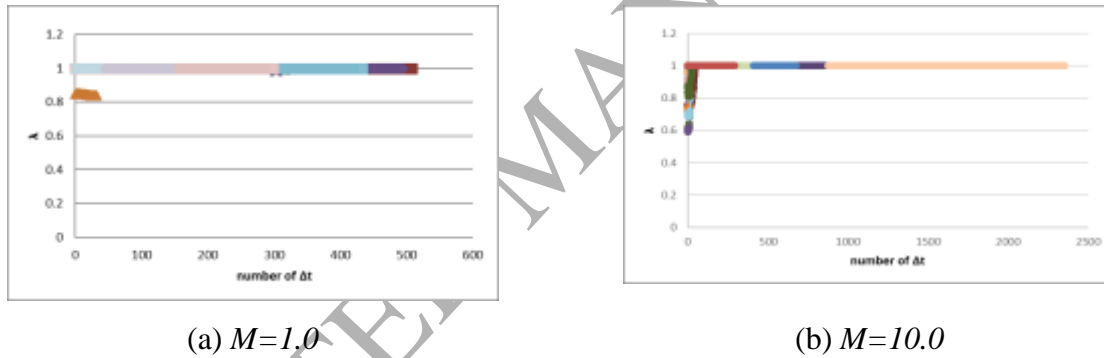

(a) *M=1.0*　　　　　　　　　　　　　　(b) *M=10.0*

Figure 20 Local Switch evolution in simulation with various viscosity ratios and ***Q=1.0e^{-8}m^3/s***, ***C$_a$=2.94e^{-4}***. Each curve represents the value of switch in a particular pore at each time step, the x-axis is the number of time steps.

IV. SUMMARY AND CONCLUSIONS

A novel dynamic model of imbibition has been presented in this paper in which three displacement mechanisms have been implemented: piston-like displacement, snap-off, and a coupled mechanism controlled by local force balance switch λ – Table 2 summarises the three local mechanisms that have been considered. The new model allows both mobile bulk menisci and swelling films to be updated simultaneously based on the local flux and time step and can be applied to a variety of network structures. To implement the impact of viscous forces correctly, capillary entry pressures must be considered when updating the global

pressure field and calculating local flow rates of pores that contain advancing menisci. A novel switch parameter, λ, has been introduced that represents the pore-level competition between capillary (snap-off) and viscous (piston-like) forces and the corresponding displacement mechanisms. This λ parameter also determines the local balance between the water film flow and bulk fluid flow in a pore element; λ is calculated *locally* in pores with bulk menisci and will vary during water imbibition. Value of λ also varies as the global rate is increased, thus potentially changing the filling mechanism from snap-off (at low flow rate), via a transitional mixed snap-off/piston-like mechanism to a piston-like mechanism (at high flow rate).

Like two phase drainage processes, imbibition processes are also governed to a considerable extent by the capillary number (C_a) and the mobility ratio *(M)*. It is well known (and reported experimentally) that there is an asymmetry between pure drainage and imbibition since there is *one* piston-like pore scale displacement mechanism in drainage (invasion percolation) and *two* mechanisms in imbibition involving piston-like and snap-off displacements. However, in imbibition processes, our simulations show that there is a "deep coupling" between viscous and capillary forces which is absent or much less important in drainage. The switch λ represents the specific relationship between local capillary entry pressure and viscous pressure drop; the actual form of λ introduced here ($\lambda = P_c /(P_c + \Delta P)$) may be changed as a consequence of future experimental observations but any alternative model must have the same limits and can be implemented trivially in our general dynamic model. The expanded form of this λ expression is given by Equation 41, which can also be expressed in terms of wettability, capillary number, viscosity ratio and aspect ratio (see Equation 43). From these two forms of λ, we can identify the parameters (or governing groups) that affect the imbibition filling regimes. This model has been implemented in 2D and 3D lattices with triangular cross-section bond elements and volume-less nodes and it includes wettability variation characterised by the local pore oil/water contact angle (θ_{ow}). However, the primary aims of this paper are (i) to present the details of the dynamic imbibition model, and (ii) to illustrate the results from it on the emergent simulated *imbibition flow regimes* using 2D network simulations. A full parametric sensitivity analysis of the resulting flow regimes has been performed but these results will be discussed in a future paper (also see Li (2016)). The illustrative 2D imbibition simulations presented here successfully reproduce many of the known observed aspects of imbibition processes. The dynamic model also demonstrates why

the various flow regimes for imbibition are different from and more complex than for corresponding drainage processes.

Influence of newly-introduced local λ can be easily observed from different types of visualizations. Furthermore, we have presented some sample results from our imbibition simulator of effluent fractional flow (f_w) and global pressure drop (ΔP) behaviour as functions of local λ. These results are sufficient to show that, when analysed to derive the unsteady-state (USS) relative permeabilities, pore-level force competition and water distribution have clearly global influences. Influences of various network and fluid parameters, including rate dependence, on USS relative permeabilities has been studied in 3D dynamic network calculations (discussed in Li (2016)) using the model proposed here and will be the subject of a future paper.

Simulation results from our full dynamic model highlight some interesting flow regimes as functions of flow rate (C_a) and mobility ratio (M = 1.0 and 10.0). This is demonstrated in Figure 21 below, which is constructed from the simulations presented above. Firstly, we can predict the impact of flow rate on water flood behaviour at adverse viscosity ratios – high rate imbibition displacements at M = 10.0 show (capillary fringed) viscous fingering behaviour (Figure 21 (d)), which transitions to capillary dominated diffusion at low rate (Figure 21 (c)). Secondly, we can show some important differences between imbibition and drainage floods at low rates: a key difference between the two is shown in the comparison between the low rate M = 1.0 and M = 10.0 cases (Figure 21 (a) and (c)). Under drainage conditions, these two floods would be expected to give identical results: clearly in imbibition they are *not* the same. The difference between these capillary dominated cases arises because of the "deep coupling" of the viscous and capillary effects during imbibition. Specifically, viscosity ratio in imbibition leads to the water wetting films having a much greater relative mobility (than oil) in the M = 10.0 case, thus giving a higher level of film swelling/snap-off, resulting in local non-wetting cluster bypassing and trapping, and hence a poorer non-wetting phase displacement. This is essentially why the microscopic displacement efficiency is lower for higher M cases in water imbibition processes. Capillary dominated pure drainage (invasion percolation) shows capillary fingering which is independent of M and this is not the case in imbibition. The physical reason as to why it is impossible to remove viscous effects during imbibition, is that capillarity is essentially *local* and of fixed magnitude, whereas viscous effects are global and must be made impractically large in realistic porous media to give a

46

local pressure gradient at the pore scale which completely overcomes capillarity. The model presented in this paper captures this central issue in the physics of imbibition.
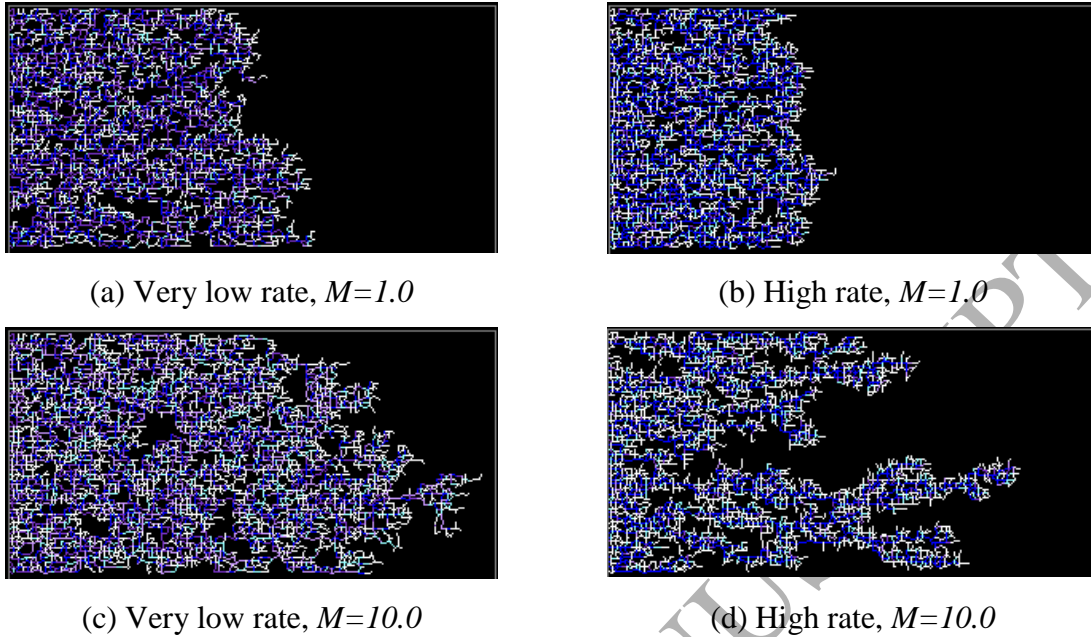

(a) Very low rate, *M=1.0*

(b) High rate, *M=1.0*

(c) Very low rate, *M=10.0*

(d) High rate, *M=10.0*

Figure 21 Summary of the simulated flow regimes for the full dynamic imbibition model (base case – date in Table 6) as a function of flow rate (Ca) and mobility ratio (M).

By correctly reproducing many of the known observed aspects of imbibition processes, our model is qualitatively validated. The current form of the switching parameter represents the linear relationship between capillary forces and viscous forces, which is able to correctly reproduce the filling regimes under different conditions. To validate or explore the more physical expression of λ, micromodel experiments could be performed at a later data to look at the distribution of incoming water and the occurrence of snap-off or pore filling within a single element under various conditions.

Future simulations using more physically-realistic, reconstructed networks could also be used to validate the model by comparing the resulting production data and relative permeabilities with the experimental data.

ACKNOWLEDGEMENT

NOMENCLATURE

Roman

A	cross-sectional area (m^2).
A_o	area occupied by bulk oil in the pore centre (m^2).
A_w	area occupied by corner water (m^2).
C_a	capillary number (-).
C_w	flow resistance factor near the pore wall (-).
d	distance a bulk menisci has travelled within a pore (m).
f	fractional flow (-).
F_d^*	Influence of pore geometry and contact angle in capillary entry pressure of piston-like displacement.
$F_d^{snap-off}$	Influence of pore geometry and contact angle in capillary entry pressure of snap-off.
g	conductance ($m^5/(N{\cdot}s)$).
G	Conductance pre unit length ($m^4/(N{\cdot}s)$).
G_{shape}	Shape factor ().
k	permeability (D).
k_{rw}, k_{ro}	water relative permeability/oil relative permeability (-).
l	pore length ($\mu m/m$).
M	viscosity ratio (-), $M = (\mu_o/\mu_w)$
n	number of arc menisci/steps (-).
n_x, n_y, n_z	number of pores in each direction (-).
P	pressure (Pa)
P_c	capillary pressure/capillary entry pressure (Pa).
ΔP	pressure drop (Pa).
Q, q	volumetric flow rate (m^3/s)
R, r	radius ($\mu m/m$).
r_w	Radius of the curvature of arc menisci (m).

R_{asp}	pore aspect ratio r/l (-).
S	saturation (-).
S_{wi}	initial water saturation (-).
S_1	A_w/r_w^2 (-).
t	time (s).
V	volume (m^3).
W	fluid hydraulic resistance
x	distance (m).
Z	coordination number (-).

Greeks

β	corner half angle (degree/radian)
Δ	difference.
μ	viscosity ((N·s)/m^2).
λ	switching parameter (-).
σ	interfacial tension ().
θ	contact angle (degree/radian).
π	3.1415926…
∇	gradient.
Σ	cross-sectional area of the network (m^2).

Subscripts

1	network inlet.
2	network outlet.
i, j	property related to node i/j, to pore i/j, or to corner i/j.
nw	Non-wetting
o	oil
t	triangle
w	water/wetting/wetting film.

Superscripts

in	flowing-in.
new	after updating.

old	before updating.
out	flowing-out.
piston-like	piston-like displacement
snap-off	displacement by snap-off

Biography

Aker, E., K. J. Maloy, A. Hansen, and G. G. Batrouni (1998). A two-dimensional network simulator for two- phase flow in porous media. *Transport in Porous Media*, 32:163–186. DOI:10.1023/A:1006510106194

Al-Gharbi, M.S., and Blunt, M.J. (2005). Dynamic network modeling of two-phase drainage in porous media. *Physical Review E* 71, 016308–016308.

Blunt, M., and King, P. (1990). Macroscopic parameters from simulations of the pore scale flow. *Physical Review A* 42, 4780–4788.

Blunt, M. (1997a). Effects of heterogeneity and wetting on relative permeability using pore level modelling. *Society of Petroleum Engineers Journal*, 2:70–87. DOI: http://dx.doi.org/10.2118/36762-PA.

Blunt, M. (1997b). Pore level modelling of the effects of wettability. *Society of Petroleum Engineers Journal*, 2:494–510. DOI: http://dx.doi.org/10.2118/38435-PA.

Fatt, I., (1956a). The network model of porous media I. Capillary pressure characteristics, *Trans AIME*, 207, 144-159.

Fatt, I., (1956b). The network model of porous media II. Dynamic properties of a single size tube network, *Trans AIME*, 207, 160-163.

Fatt, I., (1956c). The network model of porous media III. Dynamic properties of networks with tube radius distribution, *Trans AIME*, 207, 164-181.

Gielen, T., Hassanizadeh, S.M., Leijnse A., and Nordhaug, H.F. (2005). Dynamic effects in multiphase flow: A pore-scale network approach. In D.B. Das and H.S.M. (eds.),

Upscaling multiphase flow in porous media, Amsterdam, the Netherlands: Springer (pp. 217–236).

Hoshen, J. and R. Kopelman (1976). Percolation and cluster distribution. I. Cluster multiple labelling technique and critical concentration algorithm. *Phys. Rev. B* 14/8, 3438.

Hughes, R. G. and M. J. Blunt (2000). Pore scale modelling of rate effects in imbibition. *Transport in Porous Media*, 40:295–322.
DOI: http://dx.doi.org/10.1103/PhysRevB.14.3438.

Idowu, N. A. (2009). Pore-scale modelling: stochastic network generation and modelling of rate effects in waterflooding. PhD thesis. Imperial College London.

Joekar-Niasar, V., Hassanizadeh, S.M., and Dahle, H.K. (2010a). Non-equilibrium effects in capillarity and interfacial area in two-phase flow: Dynamic pore-network modeling. Journal of Fluid Mechanics 655, 38–71.

Joekar-Niasar, V., and Hassanizadeh, S.M. (2011). Effect of fluids properties on nonequilibrium capillarity effects; dynamic pore-network modeling. International Journal of Multiphase Flow 37, 198–214.

Joekar-Niasar, V. and S. M. Hassanizadeh (2012). Analysis of Fundamentals of Two-Phase Flow in Porous Media Using Dynamic Pore-Network Models: A Review, *Critical Reviews in Environmental Science and Technology*, 42:18, 1895-1976, DOI: 10.1080/10643389.2011.574101

Lenormand, R., Zarcone, C., and Sarr, A. (1983). Mechanisms of the displacement of one fluid by another in a network of capillary ducts. *Journal of Fluid Mechanics*, 135:337–353. DOI: http://dx.doi.org/10.1017/S0022112083003110.

Lenormand, R. and Zarcone, C. (1984). Role of roughness and edges during imbibition in square capillaries. Proceedings of the 59th Annual Technical Conference and Exhibition of the Society of Petroleum Engineers of AIME, SPE 13264, Houston, Texas.
DOI: http://dx.doi.org/10.2118/13264-MS

Lenormand, R. (1990), Liquids in porous media, *J. Phys. Condens. Matter*, 2(S), SA79.

Li, J. (2016), Pore-Scale Network Modelling Study to Explain the Observed Differences Between Steady-State and Unsteady-State Relative Permeabilities. PhD dissertation, Heriot-Watt U., Edinburgh.

Man, H. N. and X. D. Jing (1999). Network modeling of wettability and pore geometry effects on electrical resistivity and capillary pressure. *Journal of Petroleum Science and Engineering*, 24:255–267. DOI: 10.1023/A:1006612100346.

McDougall, S. (1994), The application of network modelling techniques to steady-and-unsteady-state multiphase flow in porous media. PhD dissertation, Heriot-Watt U., Edinburgh.

McDougall, S.R., K.S. Sorbie (1995). The impact of wettability on waterflooding: pore-scale simulation. SPE *Reservoir Engineering* August, 208– 213.
DOI: http://dx.doi.org/10.2118/25271-PA

Mogensen, K. and E. Stenby (1998). A dynamic pore scale model of imbibition. *Transport in Porous Media*, 32:299–327. DOI: http://dx.doi.org/10.2118/39658-MS.

Nguyen, V. H., A. P. Sheppard, M. A. Knackstedt, W. V. Pinczewski (2006). The effect of displacement rate on imbibition relative permeability and residual saturation. *Journal of Petroleum Science and Engineering* 52 (2006) 54-70.
DOI: 10.1016/j.petrol.2006.03.020

Øren, P.-E., S. Bakke, and O. J. Avntzen (1998). Extending predictive capabilities to network models. *Society of Petroleum Engineers Journal*, 3:324–336. DOI: http://dx.doi.org/10.2118/52052-PA.

Ryazanov, A., Pore-scale network modelling of residual oil saturation in mixed-wet system. PhD dissertation, Heriot-Watt U., Edinburgh.

Singh, M. and K. K. Mohanty (2003). Review: Dynamic modelling of drainage through three-dimensional porous materials. *Chemical Engineering Science*, 58:1–18. DOI: http://dx.doi.org/10.1016/S0009-2509(02)00438-4.

Thompson, K.E. (2002). Pore-scale modeling of fluid transport in disordered fibrous materials. *AIChE Journal* 48, 1369–1389.

Valvatne, P. H.. (2004). Predictive pore-scale modelling of multiphase flow. PhD dissertation, Imperial College London.